Upper ocean salinity balance in the western equatorial Pacific

Meghan F. Cronin and Michael J. McPhaden

NOAA, Pacific Marine Environmental Laboratory, Seattle, Washington

Abstract. The upper ocean salinity balance in the western equatorial Pacific warm pool was evaluated using up to 2.5 years of data (September 1991 through April 1994) from the Coupled Ocean-Atmosphere Response Experiment's enhanced monitoring array of moorings. At the central mooring site (0°, 156°E), precipitation had a record-length mean of 4.5 m yr^{-1}, while evaporation had a mean of 1.4 m yr^{-1}. This excess surface freshwater flux was balanced primarily by vertical mixing (estimated as the residual of a salt budget calculation) and by zonal advection. For timescales between a month and 2.5 years, surface salinity variability was dominated by zonal advection and only weakly correlated with precipitation, consistent with the concept of a zonally migrating "fresh pool." The effects of precipitation on local surface salinity variations were more apparent for timescales shorter than a month. Shallow rain "puddles" tended to form in a matter of hours. However, owing to the combination of mixing and advection, these precipitation-generated freshwater puddles were typically short-lived.

1. Introduction

The western equatorial Pacific "warm pool" is a region of very high sea surface temperature, weak trade winds, and deep atmospheric convection. With some of the highest rainfall rates found over the global ocean, it is perhaps not surprising that the region is characterized by relatively low (less than 35 practical salinity units (psu)) sea surface salinity, a fact which has led to its being called the western equatorial Pacific "fresh pool" [*Hénin et al.*, 1998]. However, it is less obvious what specific oceanic processes balance the high rain rates and on what timescales they act.

As can be seen in the time-longitude plot of the monthly averaged precipitation along the equator (Figure 1), western equatorial Pacific precipitation has interannual variability associated with El Niño-Southern Oscillation (ENSO) [*Rasmusson and Carpenter*, 1982; *Janowiak and Arkin*, 1991; *Graham and Barnett*, 1987] and intraseasonal variability associated with the Madden-Julian Oscillation [*Madden and Julian*, 1994; *Knutson and Weickmann*, 1987; *Hendon and Liebmann*, 1994; *Zhang*, 1996]. These organized convection patterns ("superclusters") have embedded in them individual convection and clusters of convection activity with higher frequency variability [*Shin et al.*, 1990; *Chen et al.*, 1996].

While one might expect that this multiscale variability in precipitation would cause a corresponding vari-

ability in the sea surface salinity (SSS) fields, *Delcroix et al.* [1996] found that in the western equatorial Pacific, seasonal SSS change was uncorrelated with precipitation. The correlation, however, was relatively large and negative (consistent with salinity variability controlled by seasonal variations in precipitation) in the central and eastern tropical Pacific. Delcroix et al.'s analysis was based on monthly maps of the tropical Pacific SSS from 15 years (1974–1989) of ship-of-opportunity data. Using this SSS data set and velocities derived from Geosat sea level height for the period November 1986 to February 1989, *Delcroix and Picaut* [1998] show that zonal advection of the SSS front separating saltier (SSS > 35 psu) central Pacific water and fresher (SSS < 35 psu) western equatorial Pacific fresh pool water was correlated with the Southern Oscillation Index of ENSO variability: During ENSO warm events, the front tended to be displaced east of the date line, and during La Niña cold events, the front was displaced westward. The large increase in surface salinity during the 1988 La Niña and subsequent freshening during the return to normal conditions in 1989–1990 was also observed by *Sprintall and McPhaden* [1994] using moored salinity time series at 0°, 165°E. Using a combination of shipboard, mooring, and drifter measurements, *McPhaden et al.* [1992] showed that southward advection of low-salinity water could also be partially responsible for the observed freshening at 0°, 165°E in late 1989.

During the past several years, there has been an increased appreciation of the role of salinity in ocean dynamics and its importance in general circulation models [*Cooper*, 1988; *Murtugudde and Busalacchi*, 1998]. Salinity, like temperature, can have a strong influence

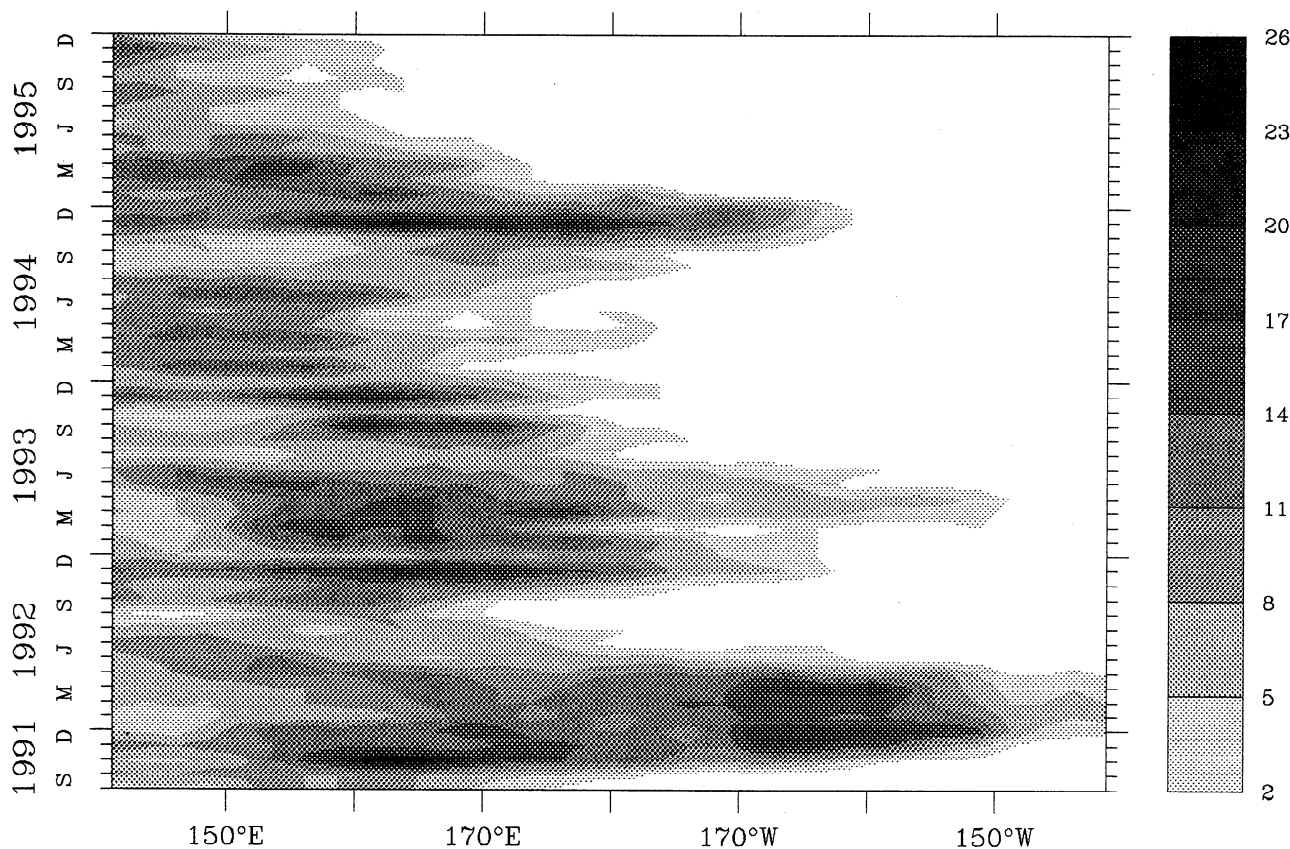**Figure 1.** Monthly averaged GOES precipitation index along 1.25°S in units of mm d^{-1}. Bin sizes are 2.5° × 2.5°.

on the buoyancy and stratification of the water column. Consequently, freshwater input can cause a shallow mixed layer that is isolated from cold thermocline water by a salt-stratified barrier layer [Godfrey and Lindstrom, 1989; Lukas and Lindstrom, 1991]. Barrier layers can inhibit cooling due to entrainment mixing. They can also affect the sea surface temperature (SST) by increasing the amount of shortwave radiation which penetrates through the layer and by changing the effective heat capacity of the water column [Anderson et al., 1996]. Additionally, salinity variations affect the formation of pressure gradients [Kessler and Taft, 1987], which potentially could be strong enough to drive zonal jets on the equator [Roemmich et al., 1994].

Understanding the multiscale processes controlling the upper ocean salinity variability in the western equatorial Pacific was a major goal of the Tropical Ocean-Global Atmosphere Coupled Ocean-Atmosphere Response Experiment (TOGA-COARE) [Webster and Lukas, 1992]. During the TOGA-COARE intensive observational period (IOP) from November 1992 through February 1993, oceanic and meteorological fieldwork was concentrated within the 150 km × 150 km intensive flux array (IFA) centered at 2°S, 156°E. TOGA-COARE studies involving salinity variability include analyses of the December 1992 westerly wind burst event [Smyth et al., 1996; Anderson et al., 1996; Feng et al., 1998], the mature phase of the October 1992 west-

erly wind burst [Wijesekera and Gregg, 1996], the life cycle of several freshwater lenses [Tomczak, 1995; Wijesekera et al., 1998], and the dynamics of surface fronts associated with freshwater lenses [Soloviev and Lukas, 1997a].

To place this mesoscale variability within the framework of larger-scale, longer-term variability, the IFA was embedded within an enhanced monitoring array (EMA) of Tropical Atmosphere Ocean (TAO) moorings for approximately 2.5 years from September 1991 through April 1994. Standard TAO measurements include hourly surface winds, air temperature, relative humidity, SST, and daily subsurface temperature on a spatial grid of approximately 10° of longitude and 2° of latitude [McPhaden, 1993]. As part of the EMA, extra TAO moorings were deployed along the equator, and several of the moorings were enhanced to measure hourly surface and subsurface temperature and salinity. The central mooring of the monitoring array (0°, 156°E) was also instrumented to monitor hourly rainfall, subsurface currents, and heat fluxes throughout most of the study period. Cronin and McPhaden [1997] (hereinafter referred to as CM97) discuss the heat balance at this location during the period from September to December, 1992, a period which spans the beginning of the TOGA-COARE intensive observational period and for which the most complete set of enhanced monitoring array observations are available.

The diagnostic analyses presented here focus on the surface layer salinity balance at 0°, 156°E for timescales ranging from hours to years. Zonal advection can be estimated from the EMA array only for timescales greater than a month, and vertical mixing cannot be directly estimated. Thus our computations of the salinity balance will necessarily be incomplete. The highly resolved IFA analyses listed above provide guidance for understanding unresolved short-timescale advective processes, as well as other unresolved processes such as turbulent mixing.

The outline of this paper is as follows. The mooring data used in this analysis are described in section 2. In section 3, the methodology for analyzing the surface layer salinity balance is discussed. Results are presented in section 4. The salinity balance during each deployment period is described, with particular attention paid to the most well-resolved period from September to December, 1992. After presenting these event analyses,

statistics of the full time series are presented. These statistics focus on the record-length mean balance and variability in the balance on a variety of timescales. For timescales less than a day, a one-dimensional mixed layer model is used to simulate the formation and dissipation of a shallow rain puddle during a period of weak surface currents. Key results are discussed and summarized in the final section.

2. Data

2.1. Buoy Array and Instrumentation

The analysis uses data from the TOGA-COARE enhanced monitoring array of TAO moored buoys (Figure 2). A few key sites (e.g., the central 0°, 156°E site) were occupied with heavily instrumented current meter moorings, referred to as profile telemetry of upper ocean currents (PROTEUS) moorings. However, most
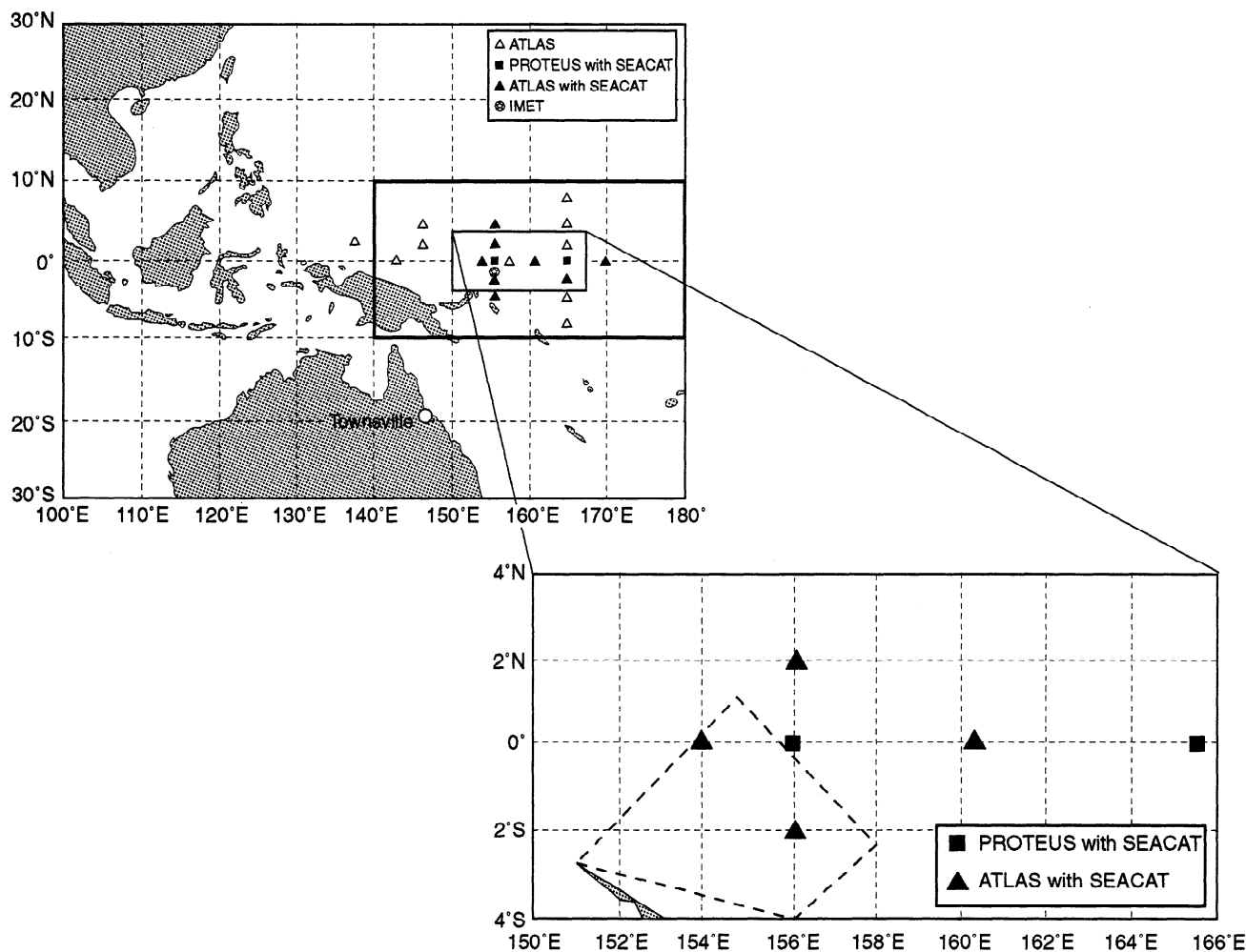

Figure 2. The Tropical Ocean-Global Atmosphere Coupled Ocean-Atmosphere Response Experiment (TOGA-COARE) enhanced monitoring array. The salinity balance is estimated at the central 0°, 156°E mooring site. Profile telemetry of upper ocean currents (PROTEUS) and Autonomous Temperature Line Acquisition System (ATLAS) moorings used in the analysis are shown in the inset. The TOGA-COARE intensive flux array (IFA) region is outlined by a dashed line.
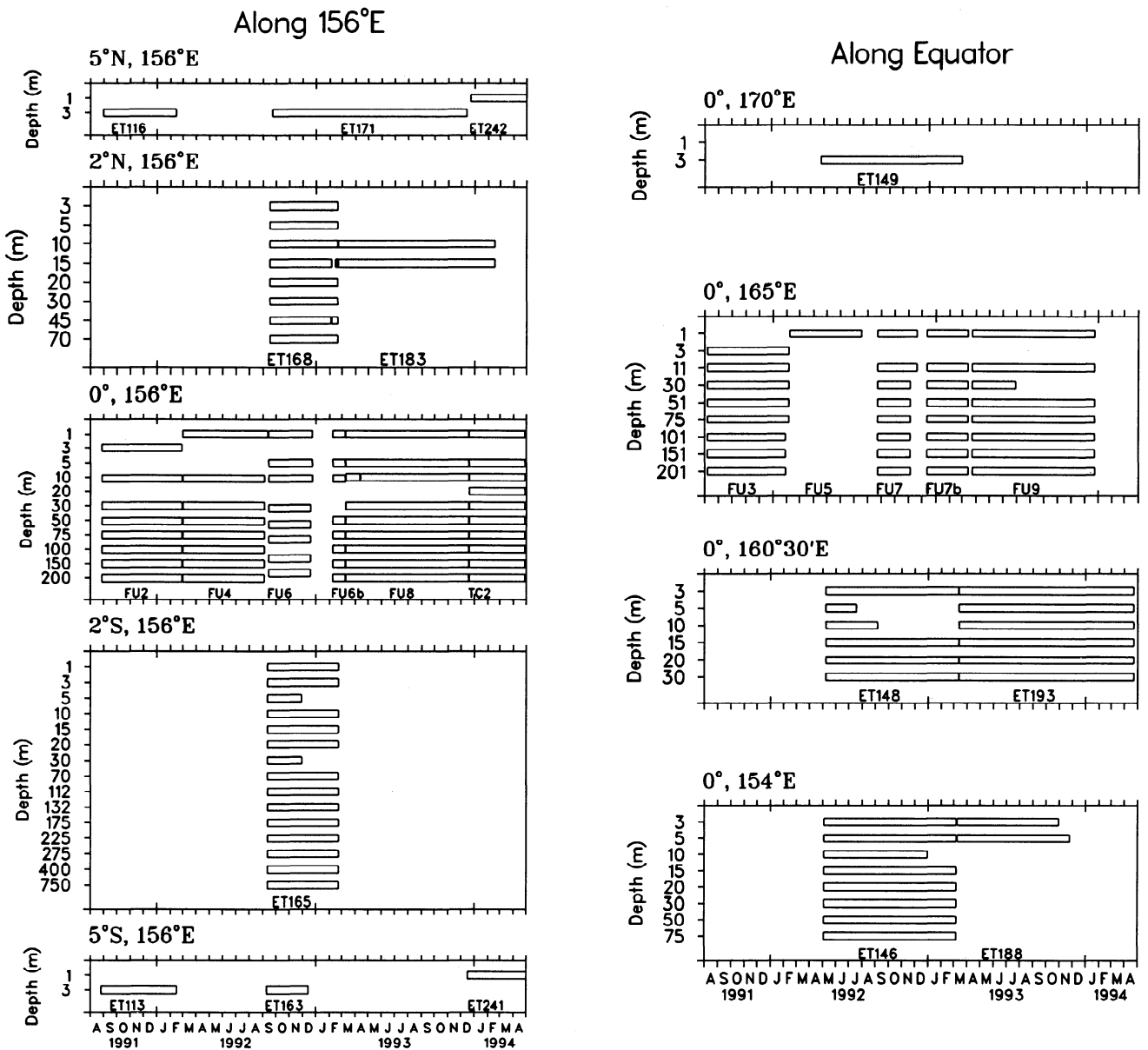
Figure 3. Depths and durations of Seabird Electronics conductivity and temperature (SEA-CAT) instrumentation from the TOGA-COARE enhanced monitoring array. SEACATs measure temperature and conductivity, from which salinity can be computed.

sites were occupied by Autonomous Temperature Line Acquisition System (ATLAS) moorings.

Seabird Electronics conductivity and temperature (SEACAT) sensors (from which salinity can be computed) were deployed on several EMA moorings (Figure 3). All moorings had a surface meteorological package which included a RM Young 05103 wind monitor and a Rotronics Instrument Corporation model MP-100 temperature-humidity probe. The heavily instrumented 0°, 156°E site had an RD Instruments downward looking 153.6-kHz acoustic doppler current profiler (ADCP) from September 1991 through February 1993, an upward looking 153.6-kHz ADCP from March 1993 through April 1994, an Epply model PSP shortwave radiometer from mid-September 1992 through April 1994, and a Science Technology model 105 op-

tical rain gauge (ORG) from March 1992 through April 1994. During the December 1993 through April 1994 deployment, two ORGs were placed on the 0°, 156°E mooring as a consistency check. For our analysis, we use the average of the duplicate ORG rain rates. A diagram of the 0°, 156°E PROTEUS buoy with full surface instrumentation is shown in Figure 4. All surface and subsurface PROTEUS data were hourly averaged and subsampled once per hour. Subsurface salinity data from nearby moorings were used only for estimates of large-scale advection and therefore were daily averaged and subsampled once per day.

2.2. Rainfall Measurements

Rainfall was measured at the central site and at five other buoy sites in the TOGA-COARE domain (0°,
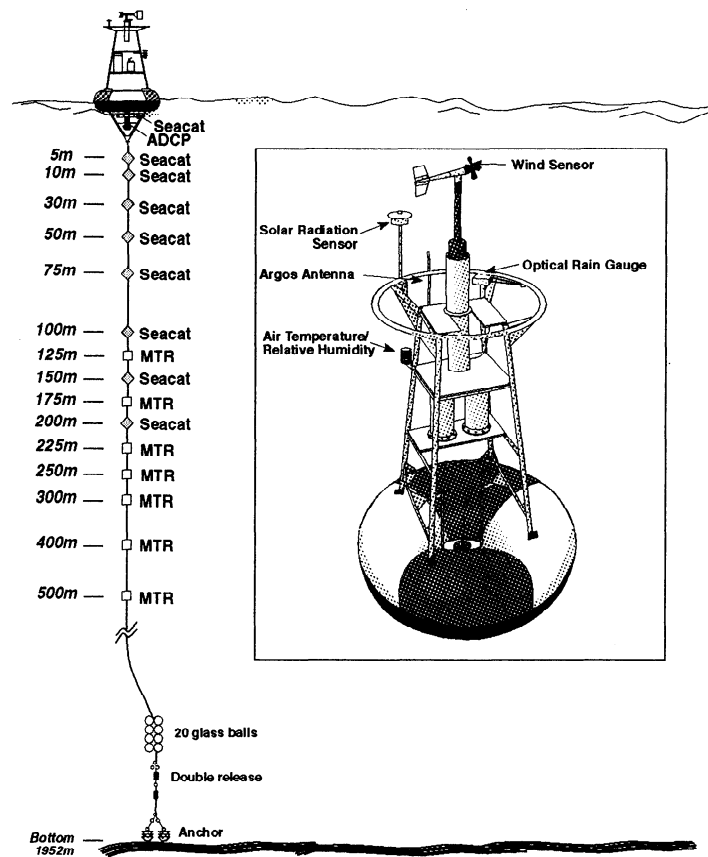
Figure 4. Diagram of the 0°, 156°E PROTEUS buoy shown with full surface instrumentation. For specific depths of SEACATs during each deployment, see Figure 3.

156°E; 0°, 154°E; 2°N, 156°E; 2°S, 156°E; 0°, 157.5°E; and 0°, 165°E) using Science Technology model 105 optical rain gauges (Figure 5). ORGs compute rain rates from scintillations caused by raindrops falling through a beam of near-infrared light with a 5-s sample rate [*Wang and Crosby*, 1993]. Hourly rain rates were computed on TAO buoys from the 5-s sample rate data and then were internally recorded and transmitted to shore in real-time via Service Argos. For details on ORG mounting, sampling, and signal-processing characteristics in TAO buoy applications, see *McPhaden and Milburn* [1992].

The accuracy of ORG rain rates has been difficult to determine for lack of sufficient calibration data in natural rain. Most of the potential ORG error sources (e.g., vibration, drop-size dependence, background environmental voltage, slanting rain, and splash from the instrument housing) would lead to relative uncertainties of $O(10\%)$. Higher relative errors are possible at low rain rates (rainfall less than 20 mm h^{-1}) and on ships which are under way [*McPhaden*, 1993; *Thiele et al.*, 1994; *Bradley and Weller*, 1996]. A cosine correction for slanting rain (C. Fairall, personal communication, 1998) could not be applied to the data since the wind speed direction relative to the ORG casing cannot be determined a posteriori on TAO buoys. However, the errors due to slanting rain and the other potential errors listed above are expected to be small relative to the uncertainty due to the factory calibrations.

For example, rain rates from the duplicate ORGs on the 0°, 156°E mooring (December 1993 through April 1994) had a cross correlation of 0.98 but a mean difference of 23%. Analyses of duplicate ORGs [*Thiele et al.*, 1994] have shown typically 15–25% differences in rain rates, although larger calibration differences have been observed in a few instances [e.g., *Short et al.*, 1997]. Thus, as done by CM97, we have assumed an ORG rain rate error of ±25%.

As described by *Bradley and Weller* [1996] and *Short et al.* [1997], TOGA-COARE IFA rainfall intercomparisons, which were based on a few mesoscale events, degraded when the spatial separation of the measurements increased beyond 7–10 km. In order to gain insight into the structure of the precipitation variability, we compared the 0°, 156°E ORG rainfall measurements with ORG data from nearby moorings. The horizontal correlation structure for precipitation was estimated using the six moored ORG time series (Figure 5) for temporal averaging intervals of 1 hour, 1 day, 5 days, and 10 days. Space lags ranged from 165 km to 1210 km. Spatial correlations increased with the temporal averaging interval (Figure 6), from near zero for hourly data at all horizontal separations (not shown) to 0.6–0.8 for 10-day averages. The near-zero correlation for hourly data is not surprising because individual rain events typically are of short duration (having a 3-hour integral time scale) and occur on spatial scales of only a few kilometers
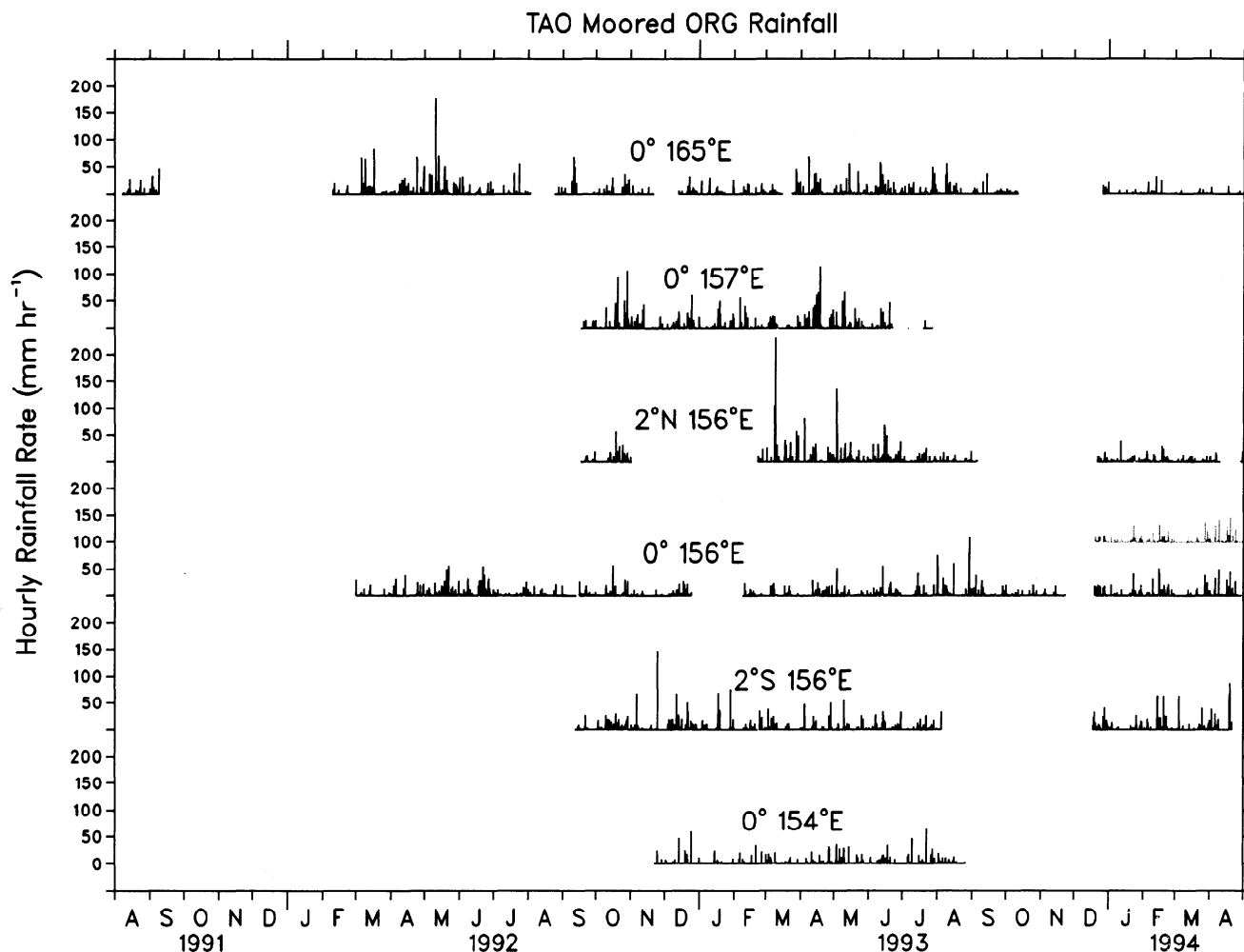
Figure 5. Time series of Tropical Atmosphere-Ocean (TAO) optical rain gauge (ORG) hourly mean precipitation at 0°, 165°E; 0°, 157.5°E; 2°N, 156°E; 0°, 156°E (data from duplicate sensor are shown in light grey); 2°S, 156°E; and 0°, 154°E.

[Short et al., 1997; Chen et al., 1996]. In general, correlations were highest at shorter spatial separation, although significantly nonzero correlations were found for 5- and 10-day averages even over 1000 km of separation. The results are consistent with the multiscale nature of the convection found in the western equatorial Pacific. As described by Chen et al. [1996], in this region, individual mesoscale convective cloud clusters often have a westward propagating envelope with near 2-day periodicity and are embedded within a larger-scale eastward propagating intraseasonal oscillation cloud envelope (sometimes referred to as a "super cloud cluster"). Large-scale patterns become more evident with increasing temporal averaging.

Because in situ rainfall measurements over the open ocean are so rare, satellite rainfall measurements are more commonly used. As reviewed by Arkin and Ardanuy [1989], satellite precipitation estimates are most accurate when averaged on timescales greater than 5 days and on spatial scales of 10^4 km^2. To obtain a similarly averaged in situ time series, a pentad composite ORG time series was computed by averaging ORG rain rates at 0°, 156°E; 0°, 157.5°E; and 2°S, 156°E.

This in situ composite is compared with three satellite precipitation data sets: GOES precipitation index (GPI), special sensor microwave/imager (SSM/I) precipitation, and microwave sounding unit (MSU) precipitation. GPI data are derived from geostationary infrared measurements of cloud top temperature and polar orbiting satellite measurements of outgoing longwave radiation flux which are regressed against direct measurements of rainfall [Janowiak and Arkin, 1991]. SSM/I and MSU rainfall estimates are derived from polar orbiting satellite microwave observations in frequency channels that are sensitive to scattering and absorption of radiation from raindrop-sized hydrometeors. The SSM/I rainfall algorithm uses the 85-, 22-, and 19-GHz channels [Ferraro et al., 1996]; MSU uses the 50-GHz channel [Spencer, 1993]. The satellite rainfall grids are coincident with 2.5° × 2.5° resolution.

Figure 7 shows the composite time series and the satellite 5-day mean rain rates for the bin centered at 1.25°S, 156°E. Although the ORG rain rates are higher than the satellite values, the ORG rain rate variability is correlated with the satellite rain rate variability (Table 1). The record-length (February 1992 through
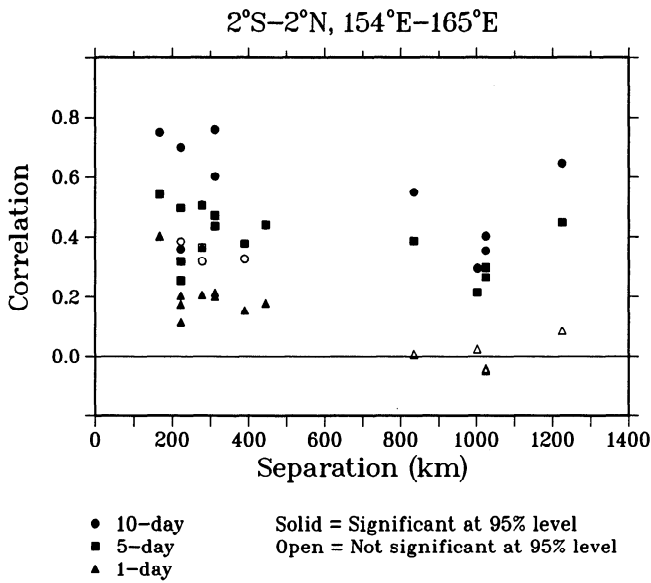
2°S–2°N, 154°E–165°E

● 10–day   Solid = Significant at 95% level
■ 5–day   Open = Not significant at 95% level
▲ 1–day

Figure 6. Spatial correlation between the six ORG precipitation time series (see Figure 5) for averaging intervals of 1 day (triangles), 5 days (squares), and 10 days (circles). Solid (open) symbols indicate the value is significant (insignificant) at the 95% confidence level. Periods when both sensors indicate no precipitation are not included in the correlation. Cross correlations with hourly data were near zero and therefore are not shown.

April 1994) rain rate at 0°, 156°E was 12.3 mm d⁻¹ as measured by the buoy ORG and 14.6 mm d⁻¹ for the three-buoy composite (0°, 156°E; 2°S, 156°E; and 0°, 157.5°E). In contrast, the mean precipitation values for the same time period from the satellite data were 10.6 mm d⁻¹ for the GPI data, 9.7 mm d⁻¹ for the SSM/I data, and 8.9 mm d⁻¹ for the MSU data. The cross correlation between the pentad 0°, 156°E ORG data and satellite values is approximately 0.5. The cross correlation is larger for the composite ORG time series (0.5–0.7) compared with the single-buoy time series, as expected. These cross correlations between ORG and satellite rain estimates are roughly equivalent to the cross correlations between the different satellite estimates (0.5 for SSM/I versus GPI and SSM/I versus MSU; and 0.8 for GPI versus MSU).

On the basis of typical ORG calibration errors and the comparison with satellite estimates of rainfall, we consider 25% to be a valid nominal error for the 0°, 156°E ORG rainfall. To test the sensitivity of our results to the choice of rainfall products and to extend the analysis beyond the ORG record length, the GPI satellite data will also be used in the salinity balance described in section 4.
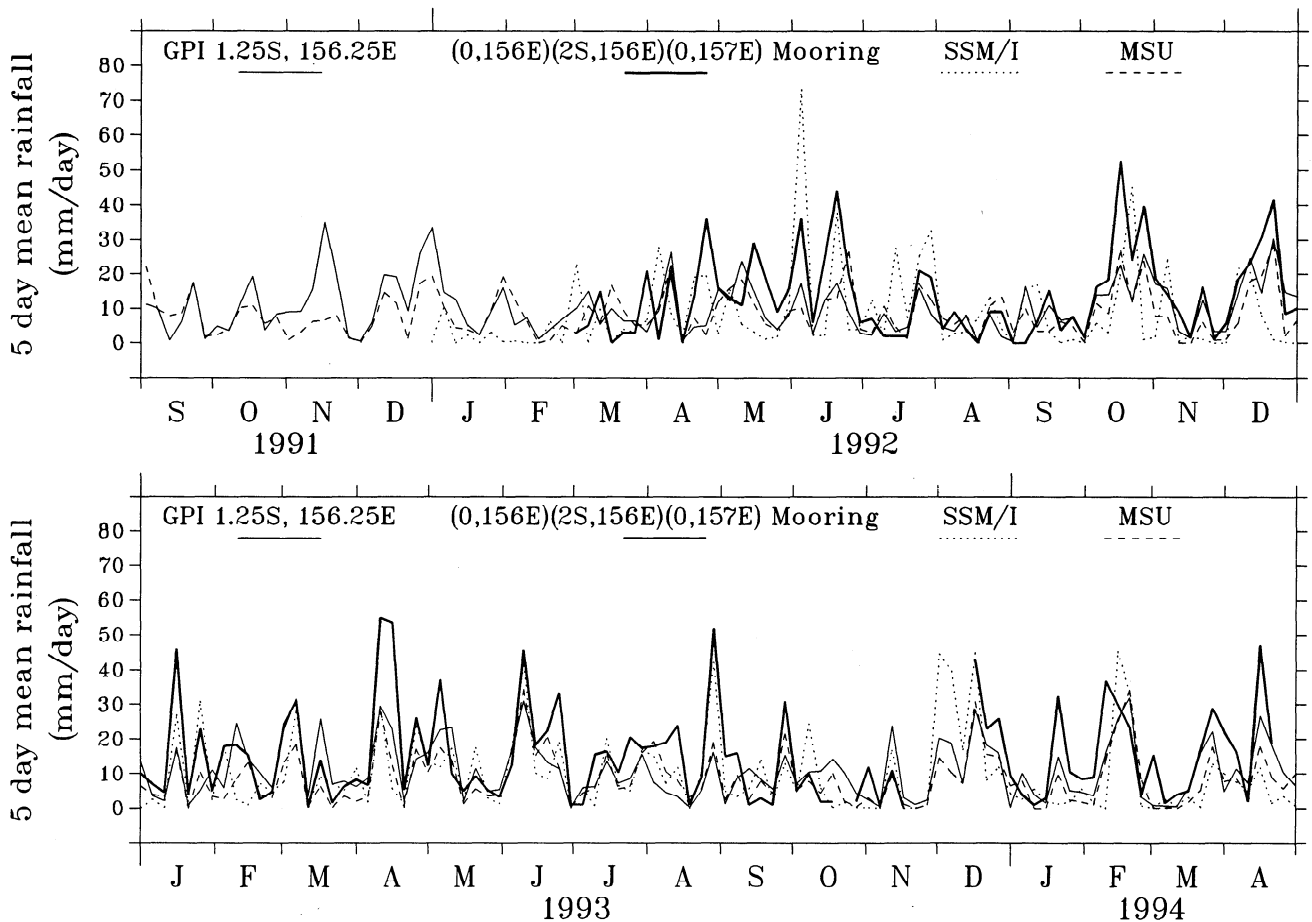

Figure 7. Pentad time series of precipitation from a composite of the 0°, 156°E; 0°, 157.5°E; and 2°S, 156°E ORGs (bold lines), GOES precipitation index (GPI) (thin lines), microwave sounding unit (MSU) (dashed lines), and special sensor microwave imager (SSMI) (dotted lines). The satellite estimates represent a 2.5° × 2.5° box centered at 1.25°S, 156°E.

Table 1. Precipitation Statistics

	Mean, mm d^{-1}	Standard Deviation, mm d^{-1}	RMS, mm d^{-1}	r_{xy}
ORG (0°, 156°E)	12.3 ± 3.1	11.7	7.2	0.8 ± 0.2
ORG (composite)	14.6 ± 3.4	13.2	0	1
GPI	10.6 ± 1.9	8.0	10.5	0.7 ± 0.2
SSM/I	9.7 ± 2.1	11.9	13.3	0.5 ± 0.2
MSU	8.9 ± 2.9	7.6	10.9	0.7 ± 0.2

All statistics are computed using pentad precipitation data from March 1992 through April 1994. Satellite precipitation are centered at 1.25°S, 156°E. The statistics include the mean value and its uncertainty at the 95% confidence level, standard deviation, and the root-mean-square difference and cross correlation with the composite ORG pentad precipitation. The uncertainty for the cross correlation represents the correlation for the null hypothesis at the 95% confidence level.

2.3. Evaporation

The rate of evaporation E is estimated from the latent heat flux Q_{lat} according to $E = Q_{lat}/(\rho L)$, where Q_{lat} is computed using the COARE bulk algorithm version 2.5b [*Fairall et al.*, 1996a; *Fairall et al.*, 1996b], L is the latent heat of evaporation, and ρ is the density of fresh water at the sea surface temperature. Figure 8 shows the daily averaged precipitation minus evaporation time series at 0°, 156°E. The record-length evaporation corresponds to a freshwater loss of 3.8 mm d^{-1}, approximately equivalent to the *da Silva et al.* [1994] climatological value of 3.5 mm d^{-1}. Over the record length, evaporation is nearly a factor of 4 smaller than the mean rain rate. Precipitation is also more highly variable than evaporation. The standard deviation of the hourly precipitation time series is 70 mm d^{-1}, over 5 times the record-length mean rain rate and 20 times the mean evaporation rate. In contrast, the standard deviation of the hourly evaporation is only 1.76 mm d^{-1}, less than half the record-length mean evaporation rate. Assuming a 10 W m^{-2} error in latent heat flux, the nominal uncertainty in evaporation is 0.36 mm d^{-1}.

2.4. Salinity Processing

Comparisons with conductivity-temperature-depth (CTD) data and comparisons of predeployment and postdeployment calibrations indicate that for deployments shorter than 6 months, SEACAT salinities have an accuracy of 0.02 psu [*McPhaden et al.*, 1990; *Sprintall and McPhaden*, 1994; H. Freitag et al., technical memo in preparation, 1998]. Several of the COARE deployments, however, were longer than 6 months and had significant changes in conductivity-cell calibration due to biofouling and scouring, particularly for sensors in the euphotic (i.e., near-surface) zone. Antifoulant plugs attached to the conductivity cells prevented biofouling for about 6 months. Past 6 months, errors in salinity increased by as much as 0.1 psu. However, with postprocessing described below, salinity accuracy for deployments longer than 6 months was improved to

nearly 0.02 psu (H. Freitag et al., technical memo in preparation, 1998).

Sensors were calibrated by Seabird prior to deployment and after the instrument recovery (if in working order). A time-dependent weighted average of these pre- and postcalibrations was used to remove a linear conductivity drift. In the postprocessing stage, residual nonlinear calibration drifts were identified and removed by analyzing the static stability of the water column (when more than one sensor was attached to the mooring) and by using temperature versus salinity characteristics measured by coincident CTD measurements. While some unstable stratification was still present in the final postprocessed data, 99% of the unstable density profiles in the corrected time series had durations of less than 3 hours and occurred between 0400 and 0600 LST, when nighttime convection is expected (H. Freitag et al., technical memo in preparation, 1998].

Figure 8 shows the postprocessed salinity stratification computed from the top three levels at 0°, 156°E (note that the depths changed from deployment to deployment). While the salinity differences are generally near zero within the mixed layer, during rain events the surface layer can become stratified by fresh water. To determine the relative effect of this freshwater flux on surface salinity variability, we evaluate the surface layer salinity balance using methodology described in the next section.

3. Methodology

The surface layer salinity balance can be written as

$$\frac{\partial S_a}{\partial t} = \frac{1}{h}S_0(E-P) - v_a \cdot \nabla S_a - \frac{1}{h}\nabla \cdot \int_{-h}^{0} \widehat{v}\widehat{S}\, dz$$

$$-\frac{1}{h}F_{-h} - \frac{1}{h}(S_a - S_{-h})\left(\frac{dh}{dt} + w_{-h}\right)$$

(1)

where S_a and v_a are the vertically averaged surface layer salinity and horizontal velocity; $\widehat{S}$ and $\widehat{v}$ are de-
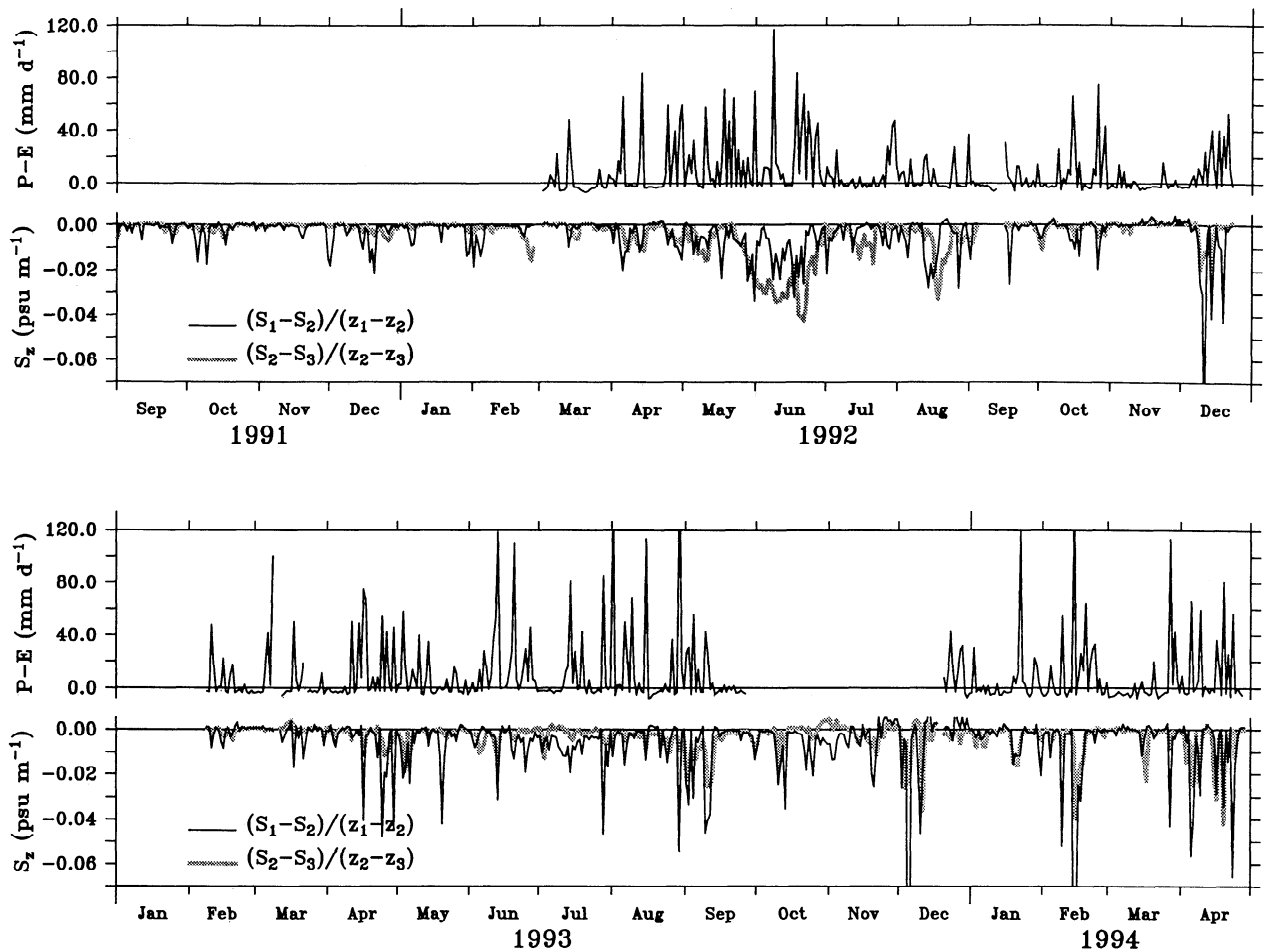
Figure 8. Daily averaged precipitation minus evaporation and daily averaged vertical salinity gradient computed from the top three levels at $0°$, $156°E$. The top three depths are as follows (see Figure 3): 3, 10, and 30 m from September 1991 through February 1992; 1, 10, and 30 m from March through August, 1992; and 1, 5, and 10 m from September 1992 through April 1994.

viations from the vertical average; S_0 and S_{-h} are the salinity at the top (taken to be $z = 1$ m) and bottom ($z = -h$) of the layer; w_{-h} is the vertical velocity at $z = -h$; E and P are the rates of evaporation and precipitation; and F_{-h} is the vertical turbulent diffusion of salinity at $z = -h$. Thus the local change in the vertically averaged salinity can be due to the dilution effect of the surface volume flux (evaporation minus precipitation), horizontal advection by the vertically averaged currents, stratified shear flow convergence, dissipation across the layer depth, and entrainment mixing.

While equation (1) is valid for any arbitrary definition of h, it is common to define h either in terms of (1) a critical density gradient or density step from the surface, (2) an isopycnal surface near the top of the pycnocline, or (3) a fixed depth. With the density step/gradient definition, the layer will be of nearly uniform density, and the corresponding S_a will be nearly equivalent to S_0 for all timescales of variability. Data with high vertical resolution [e.g., *Smyth et al.*, 1996; *Wijesekera and Gregg*, 1996; *Soloviev and Lukas*, 1997b] show that this mixed layer depth tends to have large

variability due to turbulent mixing. During periods of reduced turbulent mixing (e.g., daytime and or rain events with light wind), the mixed layer depth can be within a few centimeters to meters of the surface, while during periods of strong mixing (e.g., nighttime and/or wind bursts), the mixed layer depth can be as deep as 80 m. In contrast, a layer depth defined as a constant isopycnal surface, if deep enough, tends to behave more like a material surface, with the entrainment mixing rate (the term involving $(dh/dt + w_{-h})$ in equation (1)) approaching zero. With the constant depth h, the entrainment mixing rate reduces to a vertical advection term.

The PROTEUS mooring does not have sufficient vertical resolution to accurately estimate the mixed layer depth when it is very close to the surface. Thus, as done by CM97, we define the weakly stratified surface layer to be the portion of the water column from the ocean surface to the 21.8 kg m^{-3} isopycnal. During the occasional periods (e.g., February and March 1992) when this surface was either outcropped or shallower than 20 m, the layer depth was fixed at 20 m, approxi-
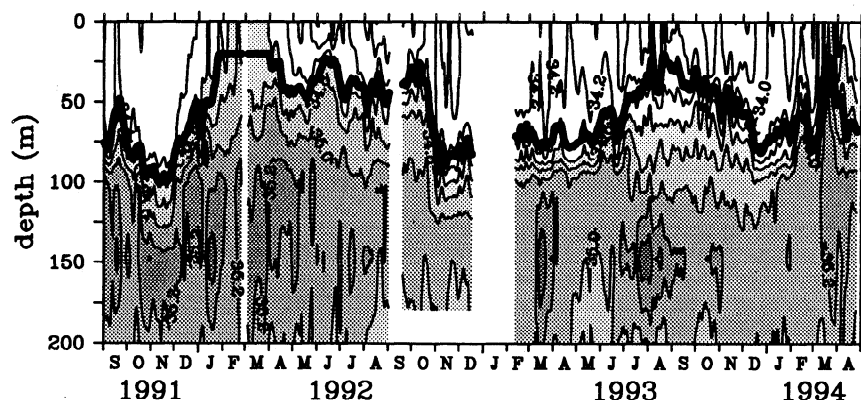
Figure 9. Five-day smoothed subsurface salinity profile time series at 0°, 156°E. The bold line is the weakly stratified surface layer depth defined by equation (2). The contour interval (C.I.) is 0.2 practical salinity units (psu).

mately the average depth of turbulent mixing [*Smyth et al.*, 1996; *Anderson et al.*, 1996; *Wijesekera and Gregg*, 1996]. Thus we define the layer depth h as

$$h = |z(\sigma = 21.8)| \quad |z(\sigma = 21.8)| > 20 \text{ m}$$
$$h = 20 \text{ m} \quad |z(\sigma = 21.8)| < 20 \text{ m} \quad (2)$$

This surface layer depth time series is superimposed upon the salinity profile time series in Figure 9, with the mean profile shown in Figure 10. The mean layer depth was 55 m, near the top of the main halocline. The high-salinity core ($S > 35$ psu) was generally 50–100 m
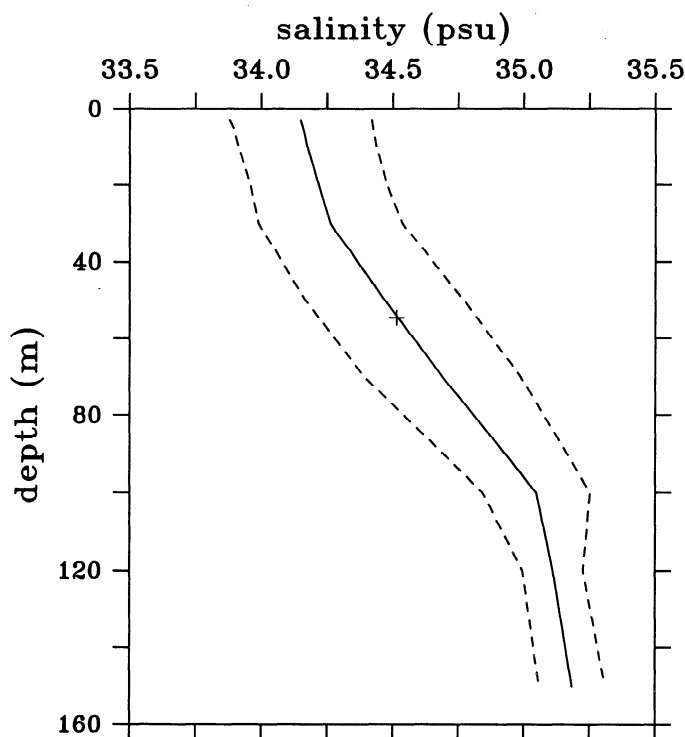
below the layer depth. The vertically averaged salinity within this surface layer, S_a, tracks the low-frequency variability of the 1-m S_0 time series but does not have the S_0 fresh spikes associated with rain events (Figures 8 and 11). Thus the weakly stratified surface layer balance (equation (1)) with the layer depth defined by an isopycnal (equation (2)) is best suited for analyzing low-frequency surface layer salinity variability.

To compute the zonal gradient, we used centered differences between the two nearest moorings east and west of 0°, 156°E if at all possible (i.e., 0°, 160.5°E minus 0°, 154°E). When data from the nearby western site (0°, 154°E) were unavailable, we used a "narrow" side difference (0°, 160.5°E minus 0°, 156°E); and when both the nearby eastern and western moorings were unavailable, we used a "wide" side difference (0°, 165°E minus 0°, 156°E) to estimate the zonal gradient at 0°, 156°E. Finally, because the 0°, 160.5°E mooring had salinity only to 30 m, advection was estimated using data only from the top 30 m. At 2°N, 156°E for the period March 1993 through mid-February 1994, salinity data are available only at 10- and 15-m depths. In this particular case, S_a was estimated by assuming salinity shallower than 10 m was equivalent to the 10 m measurement and salinity between 15 m and the base of the layer was equivalent to the 15-m measurement. If the layer was completely homogeneous, these extrapolation schemes would produce identical vertical averages. While the layer was never completely homogeneous, various other techniques for extrapolating the integration to the bottom of the layer were tested and found to give qualitatively the same result. Figures 12 and 13 show the time series of the 5-m salinity from moorings along the equator and along the 156°E longitude (at some sites this is linearly interpolated/extrapolated with respect to depth). While some of the variability at 0°, 156°E is observed at all enhanced monitoring array sites, it is clear that there are periods of large zonal and meridional surface salinity gradients, particularly in October 1992 and March 1994.
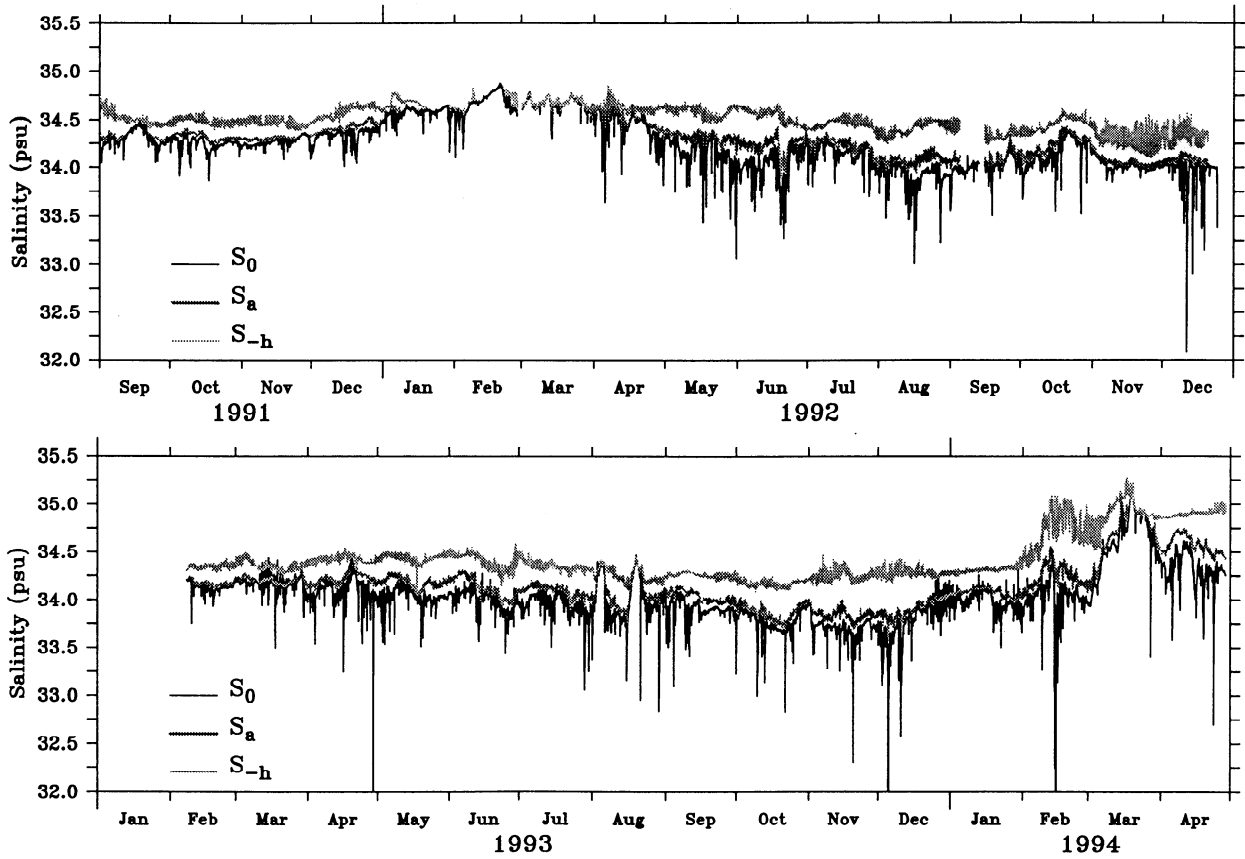

Figure 10. Record-length mean salinity profile at 0°, 156°E. The dashed lines are the ±1 standard deviation envelope. The mean layer depth defined by equation (2) is indicated by a plus sign.

Figure 11. Hourly time series of the vertically averaged weakly stratified surface layer salinity S_a, sea surface salinity at the top depth S_0 (3-m depth prior to March 1992, 1-m depth from March 1992 onward), and S at the base of the layer defined by equation (2).
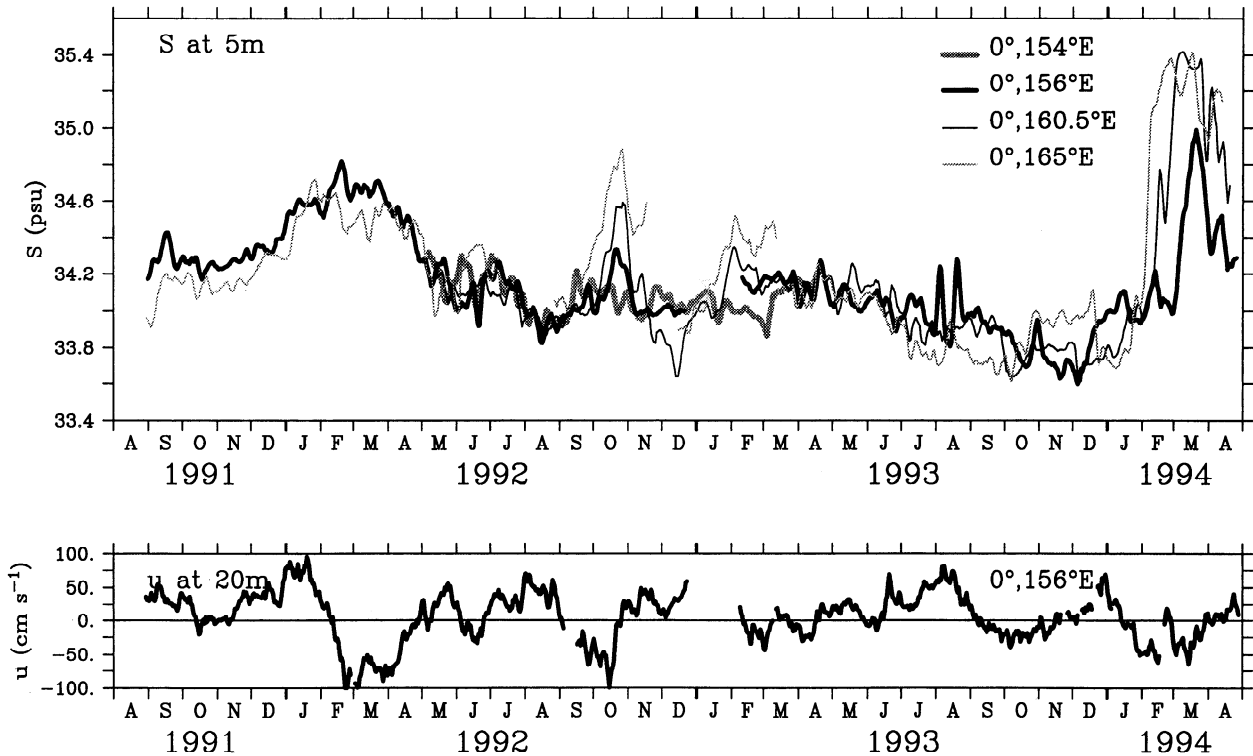
Figure 12. (Top) Five-day averaged time series of the 5-m salinity along the equator at $0°$, $154°E$; $0°$, $156°E$; $0°$, $160.5°E$; and $0°$, $165°E$. (bottom) Five-day averaged time series of the 20-m zonal current at $0°$, $156°E$.
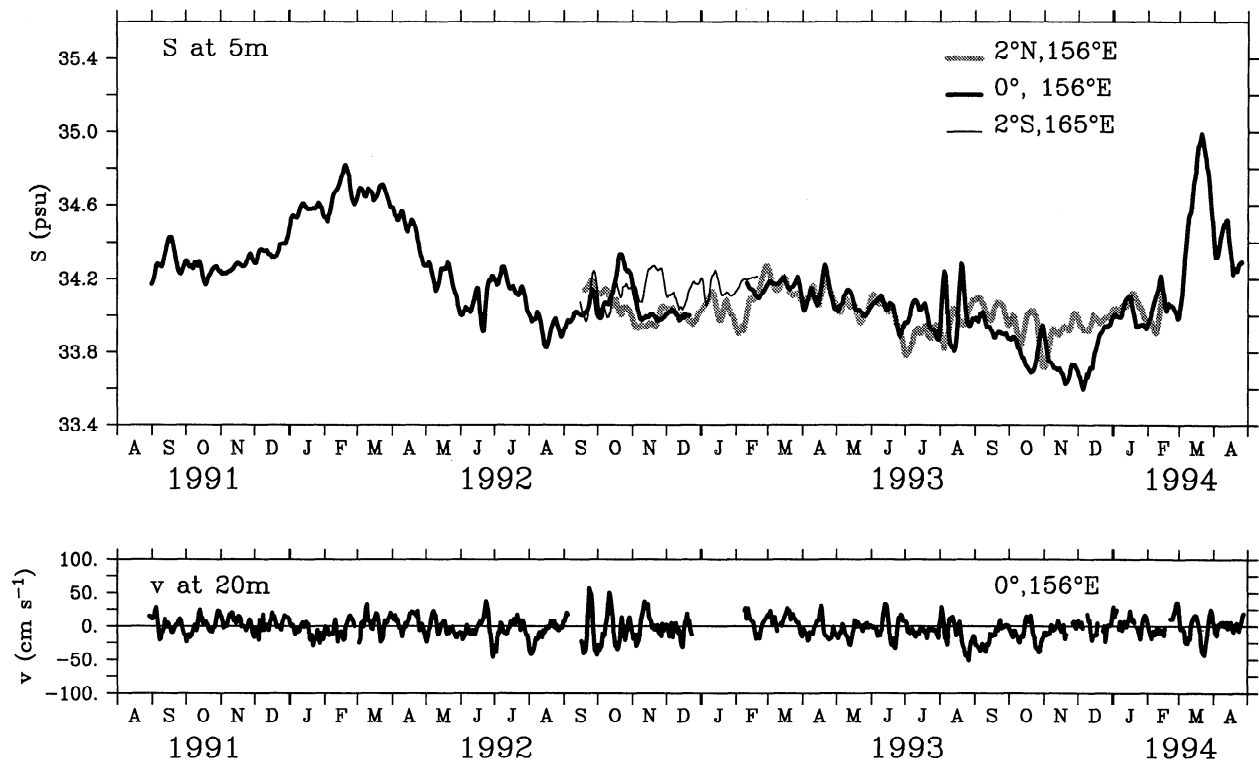
Figure 13. (top) Five-day averaged time series of the 5-m salinity along the 156°E meridian at 2°N, 156°E; 0°, 156°E; and 2°S, 156°E. (bottom) Five-day averaged time series of the 20-m meridional current at 0°, 156°E.

The convergence of salt due to sheared and stratified flow (the term involving the $\widehat{v}\widehat{S}$ in equation (1)) cannot be resolved by the mooring array and is possibly nonnegligible. Likewise, the entrainment mixing and turbulent dissipation cannot be directly measured. The combined effect of these last three terms in (1) is estimated as the left-hand side of (1) minus the first two terms of the right-hand side of (1) and will be referred to as "residual 'mixing'." Note that this residual also contains the accumulation of errors for each estimated term of (1). Thus the residual mixing term does not simply represent unresolved physical processes.

Zonal currents on the equator can be as high as 75 cm s^{-1}, and thus the minimum zonal advective timescale for the mooring array is approximately 1.5 weeks ($L/u \approx 700$ km$/75$ cm s^{-1}). However, the advective timescale is typically longer. Thus, for the weakly stratified surface layer balance, all terms in (1) were filtered with a 29-day triangular filter (15-day cutoff period, 34-day half-amplitude period) and subsampled once per day.

Error bars for each term in (1) are computed by assuming a 6-m rms error in h (see CM97); a 0.03-psu error in S_a; a 25% error in precipitation; a 0.36 mm d^{-1} error in evaporation; a 3 cm s^{-1} error in current speed; and a 2° error in current direction (CM97). The error bars for the residual term include the net effect of all the errors in the resolved processes.

For comparison, the salinity balance is also computed using the GPI pentad rainfall, P_{GPI}. To compute

E-P_{GPI} for the full 2.5-year study period, gaps in the evaporation time series (such as for the first deployment period) were filled with the mean evaporation rate. The residual mixing term estimated using the GPI precipitation will be compared with the residual based on ORG data to gain insight into the sensitivity of the residual to the choice of rainfall products.

4. Results

Because each deployment period at the central mooring site had a slightly different suite of instrumentation, we describe the results of each deployment separately. The third deployment period (September–December 1992) had the most complete data and therefore is highlighted.

4.1. First Deployment Period: September 1991 to February 1992

As shown in Figures 13 and 14, during the 3-month period from early December 1991 through February 1992, the surface salinity increased by approximately 0.55 psu from 34.3 to 34.85 psu due to zonal advection. The zonal salinity gradient, estimated with the wide side-differencing, was negative (fresher water to the east of 0°, 156°E), and surface currents were eastward (Figure 12). During this period, the 1991–1992 ENSO warm event was developing [*Kessler and McPhaden*, 1995], and the maximum rainfall was shifted eastward into the central Pacific (Figure 1).
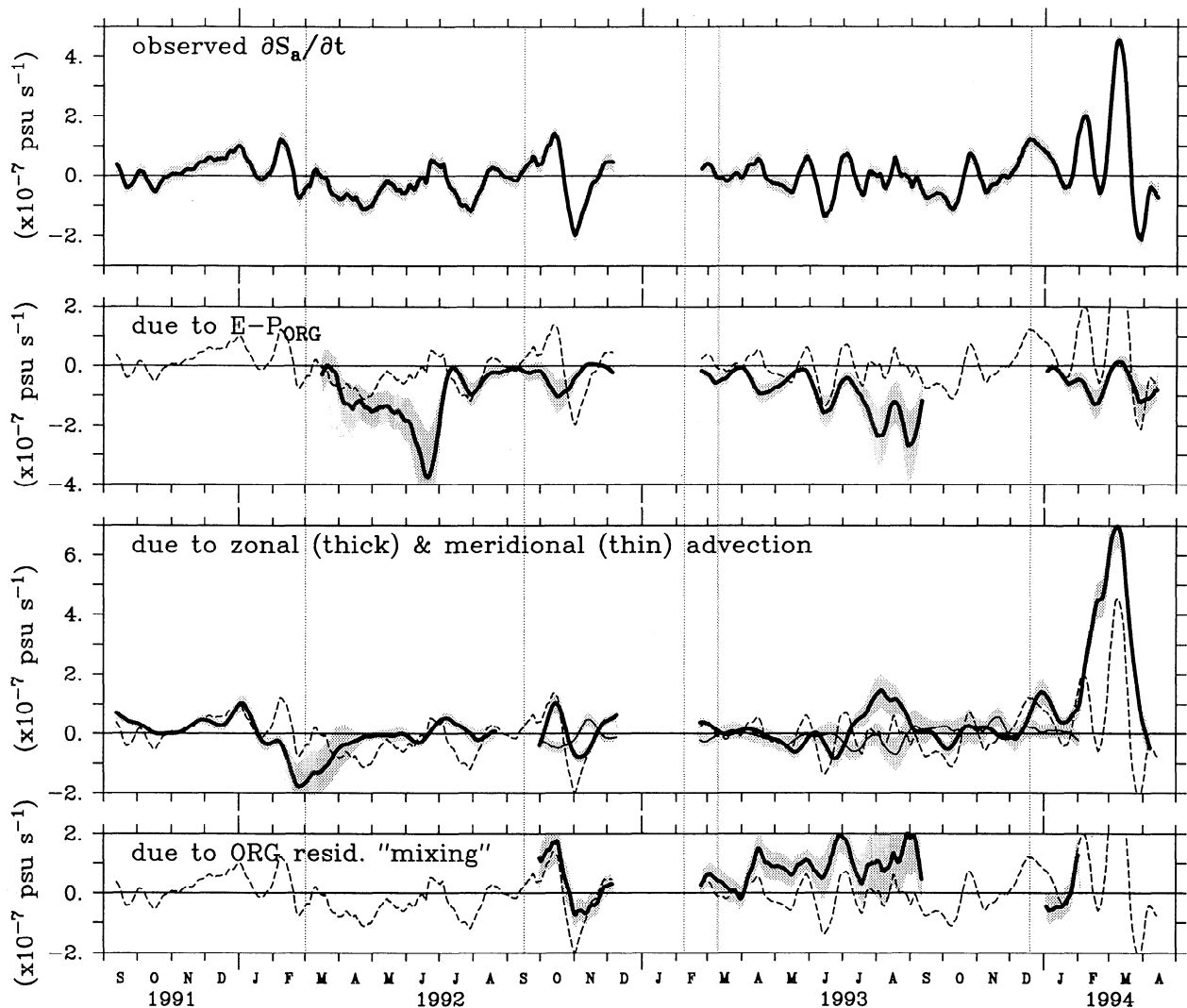
Figure 14. The 29-day low-pass filtered surface layer salinity balance at $0°$, $156°E$ in psu per second. The surface layer salinity local tendency rate is repeated as a dashed line in each panel. The ± 1 rms error for each term is indicated by the shading. The $0°$, $156°E$ deployment periods are indicated by thin vertical lines.

We suspect that the freshening due to relatively intense rain events in December 1991 to January 1992 (Figures 7 and 15) was balanced by turbulent mixing. Conditions were favorable for strong turbulent mixing during this period. As shown in Figure 9, from late November 1991 to late January 1992, the top of the pycnocline shoaled by 75 m, so that by mid-January 1992, the layer depth reached its set minimum value of 20 m. With the reservoir of salty deep water so near the surface, surface-generated turbulent energy (by wind stirring and convective overturning) could have efficiently mixed salty halocline water into the surface layer, thereby balancing the freshening due to rainfall. The residual mixing term was not computed since the meridional salinity gradient (and thus meridional advection) could not be determined. Meridional advection, however, is not expected to be a dominant process for timescales greater than a month, since the merid-

ional velocity was highly variable, changing sign often on timescales less than a month.

4.2. Second Deployment Period: March–August 1992

In February 1992, the zonal current reversed direction, and fresh water from the east was advected westward. The surface layer, however, did not freshen as quickly as would be expected from the magnitude of the zonal advection (Figure 14). Again, as shown in Figure 9, the surface layer was very shallow (20 m), and it is likely that turbulent mixing was occurring.

During the 5-month period from April through August, 1992, the 1991–1992 ENSO warm event receded, and the surface salinity steadily decreased from 34.75 to 34.05 psu (Figure 13). While the ORG rainfall was significantly larger than the GPI during this period,
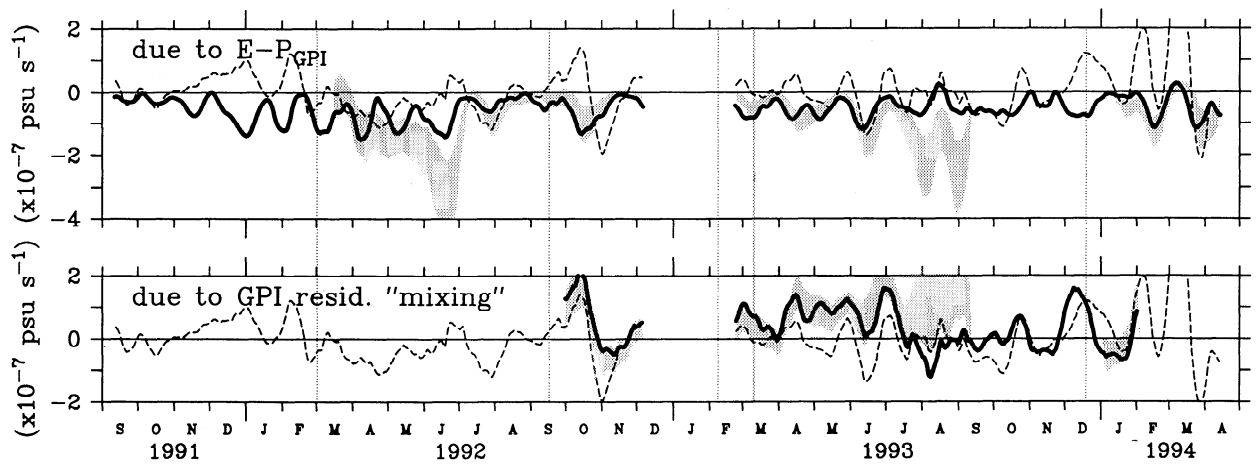
Figure 15. The 29-day low-pass filtered salinity tendency rate due to evaporation minus the GOES precipitation index at 0°, 156°E, in psu per second, and the "residual mixing" term of the salinity balance estimated using the GPI data. The observed surface layer salinity tendency rate is repeated as a dashed line in each panel. The ±1 rms error for the corresponding ORG estimated term is indicated by the shading. Since the GPI has its own errors, the rate of freshening due to the GPI is not expected to always lie within the error bars of the ORG estimate. The 0°, 156°E deployment periods are indicated by thin vertical lines.

both estimates show local precipitation as an important freshening mechanism (Figures 7, 8, 14, and 15).

4.3. Third Deployment Period: September–December 1992

The TOGA-COARE intensive observational period began on November 1, 1992. In anticipation of this, the third deployment period had the best coverage of all deployment periods. The heat balance corresponding to this deployment period is described by CM97.

October 1992 was marked by a moderately strong westerly wind burst (CM97, Figure 3), with strong rainfall during October 10–29, 1992. Nevertheless, the surface salinity increased due to the combination of zonal advection and residual mixing. A similar phenomenon was observed in the heat balance during the first part of the October 1992 wind burst: Although the surface heat flux and turbulent mixing should have caused the SST to cool, SST warmed due to zonal advection (CM97).

During the mature stage of the October 1992 westerly wind burst (October 27 to November 12) the surface layer salinity did, in fact, freshen. As shown in Figure 14, however, this freshening again appears to be due to zonal advection rather than precipitation. As can be seen in Figure 12, for the 6-week period from early October through mid-November, 1992, the zonal salinity gradient was large and positive, with high salinity values to the east of the 0°, 156°E site and low values to the west at 0°, 154°E. The change in sign of the zonal salinity advection on October 23 was due to the reversal of the surface layer current associated with the westerly wind burst. This variability in zonal advection was also evident in the heat balance (CM97).

As with the heat balance (CM97), the residual was largest in late September and mid-October, 1992. During this period, the pycnocline was extremely shallow, making entrainment mixing due to the combination of wind stirring and nighttime convection efficient mechanisms for changing the layer-averaged temperature and salinity. Because salinity increases with depth, entrainment mixing is expected to always be a positive term. The significant negative residual in early November therefore must be due to unresolved processes such as the convergence of stratified, shear flow (the term involving primed quantities in equation (1)). CM97 showed that following the October 1992 westerly wind burst, the pycnocline was deep and the near surface became stratified, conditions that favor the convergence term.

4.4. Fourth and Fifth Deployment Periods: February–December 1993

By April 1993, the 1993 ENSO warm event was evident in the eastern equatorial Pacific. In the western equatorial Pacific, from February 1993 through mid-May 1993, there was no substantial zonal salinity gradient (estimated using the centered difference), and the small variations in the surface salinity appear to be partially correlated with the evaporation minus precipitation term.

In August 1993, the 0°, 156°E ORG shows intense rainfall, which is evident in the satellite SSM/I rain product but is not evident in either the GPI or MSU fields (Figure 7). As a result, the ORG residual mixing term is positive (consistent with turbulent mixing), while the GPI residual term is negative (not consistent

with mixing) (Figures 14 and 15). Because of the lack of consistency among the satellite fields, it is unclear which rain estimate is valid for this event.

4.5. Sixth Deployment Period: December 1993 to April 1994

Cold conditions were present in the tropical Pacific during the first several months of 1994 (CM97, Figure 14). During this period, from mid-January 1994 through March 1994, the zonal salinity gradient was very strong, with central Pacific-like SSS values of over 35 psu at $0°$, $165°$E (Figure 12). The surface current was westward, associated with the South Equatorial Current. Consequently, zonal salinity advection was very large (Figure 14) and the surface salinity at $0°$, $156°$E increased by over 1 psu. This was the largest change in surface salinity during the entire 32-month record (Figure 12).

4.6. Record-Length Mean Balance

The record-length statistics for the surface layer salinity balance at $0°$, $156°$E are shown in Table 2. Note that the mean estimates are computed over the record length of each particular term, which may be longer or shorter than other terms. Thus the terms balance only within the error bars of each term.

The time-averaged tendency rate is the smallest term in the mean balance, suggesting that while there is large variability on timescales less than several months, on the 2.5-year timescale salinity is in approximate steady state. The largest term in the record-length mean balance is the freshening due to precipitation. This freshening is balanced primarily by the residual mixing term, which is nearly always positive (consistent with mixing) for both the ORG and GPI balances.

Zonal advection was the third largest term in the mean balance. Though not significant at the 95% confidence limit because of its high degree of variability, zonal advection, on average, tended to increase salinity at $0°$, $156°$E. As can be seen in Figures 12 and 13, the surface currents reverse direction frequently, resulting in a near-zero mean surface velocity. However, the gradient also changes sign. Thus decomposing the S_a advection term in (1) into time-mean and time-perturbation components, we find that the weak net advection is due primarily to the correlation of the zonal current and the zonal salinity gradient:

$$-\overline{u_a \frac{\partial S_a}{\partial x}} = -\overline{u_a}\frac{\partial S_a}{\partial x} - \overline{u_a' \frac{\partial S_a'}{\partial x}} \approx -\overline{u_a' \frac{\partial S_a'}{\partial x}}$$

Two of the largest events occurred in October 1992 and February–March 1994 when the strong South Equatorial Current advected salty water from the east. A weak reversal in the salinity gradient (i.e., fresher water to east), however, was observed in September 1991 to January 1992 and July–August 1993, when the center of the warm pool was far east of $0°$, $156°$E (CM97), associated with ENSO variability. During these periods of negative salinity gradient, the zonal current tended to be eastward, and thus salty water was advected from the west. Meridional velocity was highly variable, frequently reversing directions on timescales less than a month. Consequently, meridional advection was a very small term in the record-length mean surface salinity balance.

Table 2. Statistics of the 29-Day Low-Pass Filtered Surface Layer Salinity Balance

	Mean ($\times 10^{-8}$ psu s^{-1})	Standard Deviation ($\times 10^{-8}$ psu s^{-1})	r_{xy} With $\partial S_a/\partial t$
$\partial S_a/\partial t$	(0.20 ± 2.44)	8.29	1
$S_0(E-P_{\mathrm{ORG}})/h$	-8.49 ± 4.20	7.78	(0.23 ± 0.30)
$S_0(E-P_{\mathrm{GPI}})/h$	-5.43 ± 1.05	3.70	0.26 ± 0.24
$-u_a dS_a/dx$	(3.41 ± 6.25)	12.69	0.60 ± 0.26
$-v_a dS_a/dy$	(-0.56 ± 1.36)	2.51	(-0.16 ± 0.34)
ORG residual mixing	6.66 ± 3.83	6.95	0.45 ± 0.39
GPI residual mixing	3.60 ± 3.03	6.96	0.51 ± 0.35

The statistics include the record-length mean and its uncertainty at the 95% confidence level, standard deviation, and cross correlation with the observed upper layer salinity tendency rate. The uncertainty for the cross correlations represents the correlation for the null hypothesis at the 95% confidence level. Values in parentheses represent means and cross correlations which are insignificant at the 95% confidence level. The term residual mixing (computed as the difference between the left-hand side of equation (1) and the first two terms of the right-hand side) represents the combined effect of entrainment mixing and turbulent dissipation, convergence of salt due to sheared stratified flow, and the accumulation of errors. ORG residual mixing is computed using ORG precipitation estimates; GPI residual mixing is computed using the pentad GOES precipitation index. Note that 5×10^{-8} psu s^{-1} is equivalent to a 0.13-psu change in 30 days.

a) monthly–mean   b) daily–monthly   c) hourly–daily
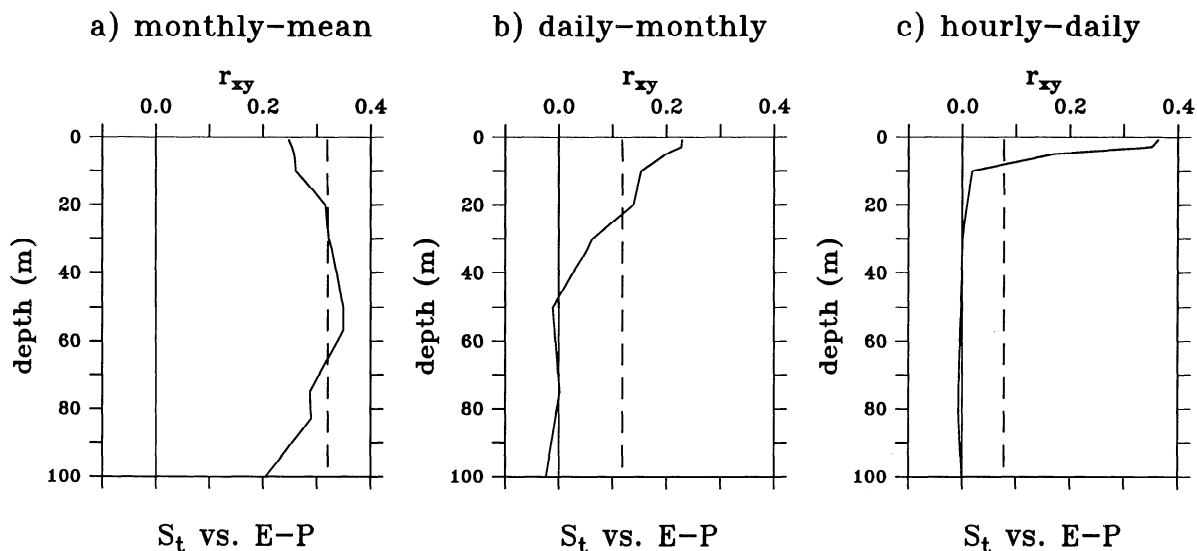

Figure 16. Correlations between evaporation minus precipitation (E-P) and the salinity tendency rate as a function of depth using (a) a 29-day low-pass filtered time series, (b) a 1- to 29-day band-pass filtered time series, and (c) a daily high-pass filtered time series. The 95% significance levels are indicated by dashed lines.

4.7. Variability on Timescales Between a Month and 2.5 Years

While precipitation was the dominant term in the record-length mean balance, zonal advection was the most prominent process responsible for variability on timescales ranging from a month to the record length, as shown by the relatively large standard deviations and cross correlations with the surface salinity tendency rate in Table 2. Residual mixing appears to be important as well. However, the S_a tendency rate was only weakly correlated with the E-P term, and E-P itself was poorly cross correlated with salinity tendency rates at individual depths in the upper 30 m (Figure 16). The relatively high cross correlation between E-P and the 50-m salinity tendency rate was probably due to Ekman pumping rather than to the surface freshwater flux. For example, Ekman downwelling is expected during westerly wind bursts which tend to occur during the convectively active periods of the Madden-Julian intraseasonal oscillation. Convectively active periods were associated not only with westerly wind bursts and high precipitation, but also with surface layer turbulence [*Wijesekera and Gregg*, 1996; *Smyth et al.*, 1996]. We suspect that the precipitation variability was partially balanced by turbulent mixing generated during convectively active wind bursts.

4.8. Variability on Timescales of a Day to a Month

To highlight processes responsible for variability on timescales between a day and a month, we band-pass filtered terms in (1) by differencing the 29-day low-pass filtered time series from the 24-hour averaged time series. Band-pass filtered advection was not computed,

however, since the mooring array's spatial resolution was too large to estimate advection for timescales less than several weeks.

The band-pass filtered layer salinity tendency rate was weakly correlated with the E-P surface flux term (0.21 ± 0.09) at the 95% confidence level, due primarily to the near-surface salinity variability (Figure 16). While surface-intensified correlations are consistent with surface rainfall freshening, with correlations of only 0.2, it is clear that other processes (e.g., lateral advection and vertical turbulent fluxes) were also occurring on these timescales.

4.9. Variability on Timescales of an Hour to a Day

4.9.1. Correlation analyses. The cross correlation between E-P and the near-surface salinity tendency rate was relatively high (0.36 ± 0.02) on timescales of an hour to a day, in comparison with the band-pass (0.21 ± 0.08) and low-pass (0.25 ± 0.3) filtered near-surface variability (Figure 16). Consistent with the formation of short-lived rain puddles, the highest near-surface salinity stratification generally occurred 1–2 hours after the peak rainfall (Figure 17). As can be seen by the large fresh spikes in the hourly 1-m salinity time series (Figure 11), this rapid precipitation freshening is followed by an almost as rapid recovery to background salinity values due to vertical mixing and/or lateral advection. The formation and erosion of short-lived rain puddles are discussed in further detail in the next section.

4.9.2. One-dimensional rain event simulations. During periods of very weak currents and weak horizontal gradients, variability is expected to be controlled by
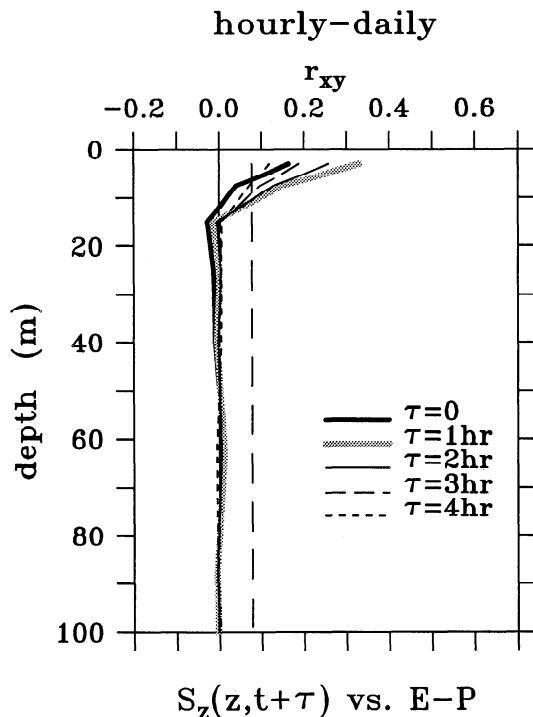
hourly–daily

r_{xy}

$S_z(z,t+\tau)$ vs. E–P

Figure 17. Correlations between evaporation minus precipitation (E–P) and the 0- to 4-hour forward shifted salinity stratification as a function of depth. All data were daily high-pass filtered. The 95% significance level is indicated by the dashed vertical line.

one-dimensional physics (e.g., surface fluxes and vertical mixing). Thus, to investigate the local formation and erosion of rain puddles, a one-dimensional mixed layer model (Price-Weller-Pinkel, or PWP) [*Price et al.*, 1986] was used to simulate the response to rainfall forcing during periods with relatively weak (10 cm s^{-1} or less) daily average surface currents. The PWP mixed layer model was initialized with CTD and ADCP data from 0°, 156°E at the start of each event and then integrated forward 48 hours with the observed hourly surface fluxes of heat, moisture, and momentum, as done CM97. A linear drag function ($-Cu$) with an e-folding timescale of 7 days was included in the momentum balance to account for unresolved dynamics such as the zonal pressure gradient, although it had little effect on the 48-hour integration. The surface turbulent fluxes (wind stress, and latent and sensible heat fluxes) were computed using the COARE version 2.5b bulk algorithm, shortwave radiation was directly measured by an Epply shortwave radiometer, and longwave radiation was estimated using the *Clark et al.* [1974] algorithm, with cloud fraction estimated from the daily averaged shortwave radiation measurements (see CM97 for more detail).

We will discuss only one event from the deployment, January 22, 1994, which had two ORGs and the highest vertical resolution salinity data. As with the empirical analysis, the model was run with the average of the two ORG precipitation measurements. During middle

to late January 1994, the surface currents and salinity gradients changed sign and therefore were weak (Figures 12 and 13). Consequently, the salinity balance is expected to be near one-dimensional during this period.

As can be seen in Figure 18, the rainfall began at 1800 GMT, January 22, 1994 (0400 LST, January 23), with rates as high as 35 mm h^{-1} and tapered off to trace values by 0300 GMT, January 23 (1300 LST). A deepening lobe of fresh water is clearly defined in the simulation and the observations. As the lobe deepened, subsurface salinity decreased and surface 1-m salinity increased. Thus freshening at 1 m occurred only during the first 1–2 hours of the 9-hour rain event. By 1200 GMT (2200 LST), 18 hours after the rain began, the freshwater puddle had completely eroded.

Because the model does not include internal wave dynamics, the simulated layer depth was essentially constant, while the observed layer depth varied by as much as 15 m and, in particular, deepened during the event. Consequently, as shown in Figure 19, the simulated dilution due to the rain event was slightly stronger than would be expected in the observed layer. However, the observations show that the layer defined by (2) freshened by 0.06 psu, approximately equivalent to the dilution due to the measured precipitation.

While this case study shows how local processes (rainfall and mixing) can form short-lived fresh puddles, near one-dimensional events are relatively rare on the equator where surface zonal jets are typically stronger than 25 cm s^{-1}. Of the 685 days in which rain rates were measured at 0°, 156°E, 259 days (38% of record) had rain rates greater than 6 mm d^{-1}, but only 22 days (3%) had both rain rates higher than 6 mm d^{-1} and daily averaged surface currents less than 10 cm s^{-1}. In total, there were 25 rain events satisfying our one-dimensional criteria. Currents also have considerable variability on timescales less than a day due to tides, and so instantaneously, the currents could be larger than the 10 cm s^{-1} daily average criterion, and even a 10 cm s^{-1} current can have an order 1 influence on salinity if it advects a sharp front past the buoy. *Soloviev and Lukas* [1997a] observed surface fronts with widths of 1–100 m separated at distances of 0.2–60 km in the western equatorial Pacific. Thus, in addition to the freshwater fluxes at the surface, both vertical mixing and lateral advection are expected to be of importance for the surface salinity variability on these short timescales.

5. Summary and Conclusion

This study has analyzed the upper ocean salinity balance in the western equatorial Pacific using COARE enhanced monitoring array data. The region is characterized by very high precipitation rates, and the 2-year period from March 1992 to April 1994 appears to have been particularly wet. Satellite (GPI, SSM/I, and MSU) rainfall over the central site (0°, 156°E) was approximately 10–20% higher during this 2-year period
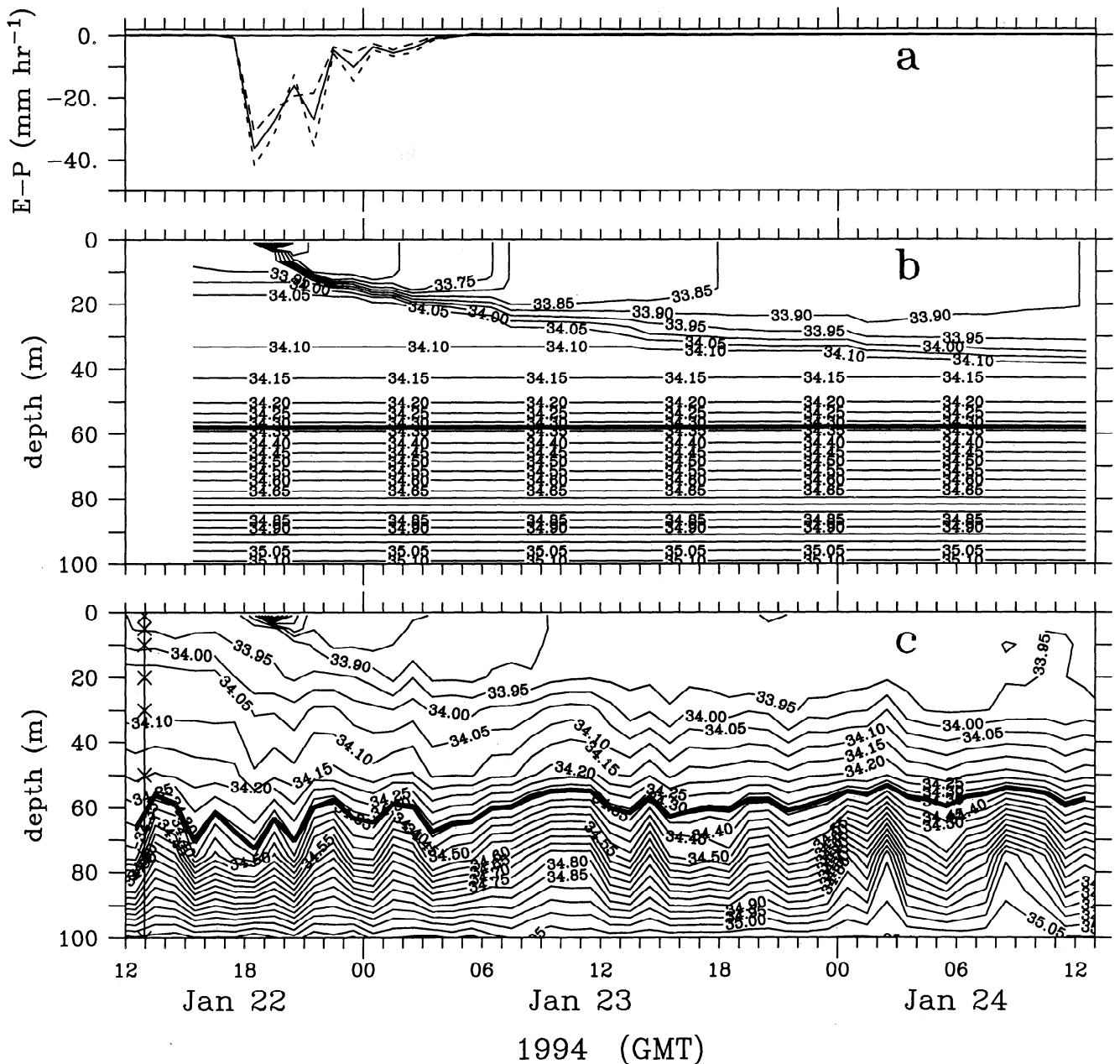
Figure 18. Simulation of a rain event using the Price-Weller-Pinkel one-dimensional mixed layer model. Rainfall begins at 1800 GMT, January 22, 1994 (0040 LST, January 23, 1994). (a) Observed $E-P$ using rain rates from the two $0°$, $156°E$ ORGs (dashed lines) and the average between the two ORG rain rates (solid line). (b) Simulated salinity stratification subsampled to 2-m resolution. The C.I. is 0.05 psu. The solid line is the simulated surface layer depth as defined by equation (2), i.e., the depth at which the simulated density is 21.8 kg m^{-3}. (c) Observed salinity stratification. The C.I. is 0.05 psu. The solid line is the observed surface layer depth as defined by equation (2).

than during their respective 10-year climatologies for 1987–1996. At the central mooring site ($0°$, $156°E$) the March 1992 to April 1994 2-year mean precipitation measured by optical rain gauges was 12.8 mm d^{-1} (4.5 m yr^{-1}), and mean evaporation was 3.8 mm d^{-1} (1.4 m yr^{-1}) . While the ORG mean rain rate was higher than the satellite 2-year mean values, ORG and satellite pentad rainfall were well correlated (Table 1). Both ORG and satellite rain rates produced realistic ocean salinity

balances, with slightly higher inferred mixing rates for the ORG balance.

Over the record length, the excess fresh water precipitated at $0°$, $156°E$ was balanced by residual processes (presumably entrainment mixing) and by zonal advection. As with the mean zonal heat advection [Ralph et al., 1997], mean zonal salinity advection occurred through the correlation of transient zonal flow and zonal salinity gradients, rather than through a mean flow
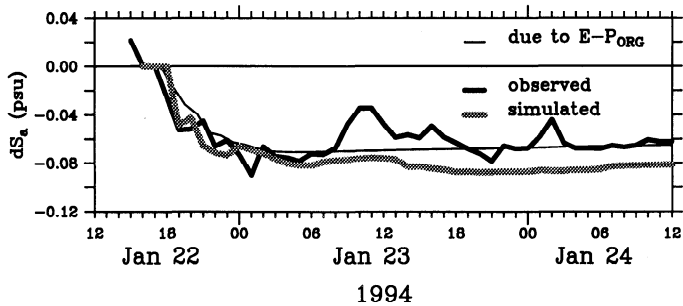
Figure 19. Accumulated salt fluxes in the layer above the 21.8 kg m^{-3} density surface (surface layer) during the rain event shown in Figure 18.

across a mean gradient. Perhaps not surprisingly, the zonal salinity advection had substantial variability, and for timescales between a month and 2.5 years, surface salinity variability was predominantly due to zonal advection. While there was substantial variability in the rainfall associated with the Madden-Julian intraseasonal oscillation, this variability was only weakly correlated with the local surface salinity variability. During the TOGA-COARE intensive observational period, turbulent mixing increased during the convectively active periods of the intraseasonal oscillation [*Wijesekera and Gregg*, 1996; *Smyth et al.*, 1996]. Thus presumably turbulent mixing partially balanced the surface freshwater flux on these timescales.

The importance of zonal advection on timescales longer than a month was also found by *Delcroix et al.* [1996], *Hénin et al.* [1998], and *Delcroix and Picaut* [1998] using ship-of-opportunity surface salinity data. Their analyses show that a sharp SSS front separating saltier central Pacific water and fresher western equatorial Pacific waters is advected zonally in phase with the Southern Oscillation Index. In contrast to the western Pacific region, where precipitation dominates over evaporation and surface currents are often driven eastward by westerly wind bursts, in the central Pacific evaporation dominates over precipitation and surface currents are driven westward by the easterly trade winds. Using the Laboratoire d'Oceanographie Dynamique et de Climatologie (LODYC) ocean general circulation model, *Vialard and Delecluse* [1998] show that the SSS front separating the central and western equatorial Pacific waters is formed by the convergence of fresh eastward currents and the saltier westward South Equatorial Current. Curiously, the model also reproduced a much weaker but still significant negative SSS zonal gradient in the far western Pacific, presumably due to the zonal gradient in the rainfall (see Figure 1). As conceptualized by *Hénin et al.* [1998] (see their Figure 10), the large-scale western equatorial Pacific surface salinity field can be viewed as a zonally migrating "fresh pool" with a sharp front on the eastern edge and a much weaker gradient on the western edge. This negative salinity gradient associated with the fresh pool's western edge is not evident in climatologies [*Levitus and*

Boyer, 1994], probably because it is both weak and transient. The data presented here were used in the *Hénin et al.* [1998] analysis and represent one of the few observations of the fresh pool's weak western edge.

The effects of precipitation on local surface salinity variations were more apparent for timescales shorter than a month. Shallow rain "puddles" tended to form in a matter of hours. Rain events producing these puddles were typically short and episodic, having an integral timescale of only 3 hours. Lagged correlations show that the rain puddle's near-surface freshwater stratification generally was strongest 1-2 hours after the peak rainfall.

A barrier layer between the shallow halocline and deeper thermocline is a feature of the western Pacific climatology [*Sprintall and Tomczak*, 1992; *Ando and McPhaden*, 1997]. As the name implies, barrier layers inhibit mixing of heat. However, mixing of salinity into the surface layer is not inhibited and, in fact, may be enhanced since the layer is stratified only by salinity. Although turbulent mixing was not directly measured in our analysis, a residual mixing term was computed by subtracting the estimated net surface flux and lateral advection from the local tendency rate. The residual mixing rates, estimated with the ORG rainfall and the pentad GPI rain rates, were nearly always positive, indicating a source of high salinity consistent with mixing. The residual mixing rates were also significantly correlated with the local tendency rate. Mixing appears to be an important process in the surface salinity balance for all timescales.

Microstructure measurements taken during the TOGA-COARE IOP show a near balance between the dilution rate due to a rain event and dissipation across the shallow mixed layer depth [*Smyth et al.*, 1996]. Over the duration of a wind burst, dissipation across the top of the pycnocline (i.e., the 22 kg m^{-3} isopycnal surface) could not compensate for the accumulation of fresh water, and thus the authors assume that lateral advection was responsible for salinity variations in the shallow mixed layer and for maintaining the salinity balance within the upper ocean layer. Making repeat zonal and meridional sections in this region (2°S, 156°E), *Huyer et al.* [1997] observed a northward migrating salinity front, presumably associated with westerly wind induced equatorial Ekman transport. Using these sections, *Feng et al.* [1998] computed horizontal salinity advection and showed that it was of the correct sign and magnitude to close the salinity budget. With strong transient surface currents and salinity fronts ranging in width from several meters [*Soloviev and Lukas*, 1997a] to over 1000 km [*Hénin et al.*, 1998; *Delcroix and Picaut*, 1998], lateral advection is a crucial component of the salinity balance in the western equatorial Pacific.

This study has evaluated the surface salinity balance at 0°, 156°E in the western equatorial Pacific for timescales ranging from hours to years. Rainfall, vertical mixing, and lateral advection were important

processes on all timescales. Zonal advection, in particular, tended to control the local salinity variability for timescales greater than a month and was consistent with the concept of a zonally migrating "fresh pool."

References

Anderson, S. P., R. A. Weller, and R. B. Lukas, Surface buoyancy forcing and the mixed layer of the western Pacific warm pool: Observations and 1-d model results, *J. Clim.*, *9*, 3056–3085, 1996.

Ando, K., and M. J. McPhaden, Variability of surface layer hydrography in the tropical Pacific Ocean, *J. Geophys. Res.*, *102*, 23,063–23,078, 1997.

Arkin, P. A., and P. E. Ardanuy, Estimating climate-scale precipitation from space: A review, *J. Clim.*, *2*, 1229–1238, 1989.

Bradley, F., and R. Weller (Eds.), Fourth workshop of the TOGA COARE air-sea interaction flux working group, 72 pp., Woods Hole Oceanogr. Inst., Woods Hole, Mass., 1996.

Chen, S. S., R. A. Houze Jr., and B. E. Mapes, Multiscale variability of deep convection in relation to large-scale circulation in TOGA COARE, *J. Atmos. Sci.*, *53*, 1380–1409, 1996.

Clark, N.E., L. Eber, R. M. Laurs, J. A. Renner, and J. F. T. Saur, Heat exchange between ocean and atmosphere in the eastern North Pacific for 1961–71, *NOAA Tech. Rep. NMFS SSRF-682*, 108 pp., 1974.

Cooper, N. S., The effect of salinity on tropical ocean models, *J. Phys. Oceanogr.*, *18*, 697–707, 1988.

Cronin, M. F., and M. J. McPhaden, The upper ocean heat balance in the western equatorial Pacific warm pool during September–December 1992, *J. Geophys. Res.*, *102*, 8533–8553, 1997.

da Silva, A., A. C. Young, and S. Levitus, Atlas of Surface Marine Data 1994, vol. 1, Algorithms and Procedures, *NOAA Atlas NESDIS 6*, 83 pp., U. S. Dep. of Commer., Washington, D. C., 1994.

Delcroix, T., and J. Picaut, Zonal displacement of the western equatorial Pacific "fresh pool," *J. Geophys. Res.*, *103*, 1087–1098, 1998.

Delcroix, T., C. Hénin, V. Porte, and P. Arkin, Precipitation and sea-surface salinity in the tropical Pacific Ocean, *Deep Sea Res., Part I*, *43*, 1123–1141, 1996.

Fairall, C., E. F. Bradley, J. S. Godfrey, G. A. Wick, J. B. Edson, and G. S. Young, Cool-skin and warm-layer effects on sea surface temperature, *J. Geophys. Res.*, *101*, 1295–1308, 1996a.

Fairall, C., E. F. Bradley, D. P. Rogers, J. B. Edson, and G. S. Young, Bulk parameterization of air-sea fluxes for Tropical Ocean-Global Atmosphere Coupled-Ocean At-

mosphere Response Experiment, *J. Geophys. Res.*, *101*, 3747–3764, 1996b.

Feng, M., P. Hacker, and R. Lukas, Upper ocean heat and salt balances in response to a westerly wind burst in the western equatorial Pacific during TOGA COARE, *J. Geophys. Res.*, *103*, 10,289–10,311, 1998.

Ferraro, R. R., F. Weng, N. C. Grody, and A. Basist, An eight-year (1987–1994) time series of rainfall, clouds, water vapor, snow cover, and sea ice derived from SSM/I measurements, *Bull. Am. Meteorol. Soc.*, *77*, 891–904, 1996.

Godfrey, J. S., and E. J. Lindstrom, The heat budget of the equatorial western Pacific surface mixed layer, *J. Geophys. Res.*, *94*, 8007–8017, 1989.

Graham, N. E., and T. P. Barnett, Sea surface temperature, surface wind divergence, and convection over tropical oceans, *Science*, *238*, 657–659, 1987.

Hendon, H. H., and B. Leibmann, Organization of convection within the Madden-Julian oscillation, *J. Geophys. Res.*, *99*, 8073–8083, 1994.

Hénin, C., Y. du Penhoat, and M. Ioualalen, Observations of sea surface salinity in the western Pacific fresh pool: Large-scale changes in 1992–1995, *J. Geophys. Res.*, *103*, 7523–7536, 1998.

Huyer, A., P. M. Kosro, R. Lukas, and P. Hacker, Upper ocean thermohaline fields near 2°S, 156°E, during Tropical Ocean-Global Atmosphere-Coupled Ocean-Atmosphere Response Experiment, November 1992 to February 1993, *J. Geophys. Res.*, *102*, 12,749–12,784, 1997.

Janowiak, J. E., and P. A. Arkin, Rainfall variations in the tropics during 1986–1989, as estimated from observations of cloud-top temperature, *J. Geophys. Res., suppl.*, *96*, 3359–3373, 1991.

Kessler, W. S., and M. J. McPhaden, The 1991–1993 El Niño in the central Pacific, *Deep Sea Res., Part II*, *42*, 295–333, 1995.

Kessler, W. S., and B. A. Taft, Dynamic heights and zonal geostrophic transports in the central tropical Pacific during 1979–84, *J. Phys. Oceanogr.*, *17*, 97–122, 1987.

Knutson, T. R., and K. M. Weickmann, 30–60 day atmospheric oscillations: Composite life cycles of convection and circulation anomalies, *Mon. Weather Rev.*, *115*, 1407–1436, 1987.

Levitus, S., and T. P. Boyer, *World Ocean Atlas 1994, vol. 3, Salinity*, NOAA Atlas NESDIS 3, 97 pp., U. S. Dep. of Commer., Washington, D. C., 1994.

Lukas, R., and E. Lindstrom, The mixed layer of the western equatorial Pacific Ocean, *J. Geophys. Res., suppl.*, *96*, 3343–3357, 1991.

Madden, R. A., and P. R. Julian, Observations of the 40–50-day tropical oscillation—A review, *Mon. Weather Rev.*, *122*, 814–837, 1994.

McPhaden, M. J., TOGA-COARE optical rain gauge measurements, workshop report, *TOGA Notes*, *13*(18–19), Nova Southeastern Univ. Oceanogr. Cent., Dania, Fla., 1993.

McPhaden, M. J., and H. B. Milburn, Moored precipitation measurements for TOGA, *TOGA Notes*, *7*(1–5), Nova Southeastern Univ. Oceanogr. Cent., Dania, Fla., 1992.

McPhaden, M. J., H. P. Freitag, and A. J. Shepherd, Moored salinity time series measurements at 0°, 140°W, *J. Atmos. Oceanic Technol.*, *7*, 568–575, 1990.

McPhaden, M. J., F. Bahr, Y. du Penhoat, E. Firing, S. P. Hayes, P. P. Niiler, P. L. Richardson, and J. M. Toole, The response of the western equatorial Pacific Ocean to westerly wind bursts during November 1989 to January 1990, *J. Geophys. Res.*, *97*, 14,289–14,303, 1992.

Murtugudde, R., and A. J. Busalacchi, Salinity effects in a tropical ocean model, *J. Geophys. Res.*, *103*, 3283–3300, 1998.

Price, J., R. Weller, and R. Pinkel, Diurnal cycling: Observations and models of upper ocean response to diurnal heating, cooling, and wind mixing, *J. Geophys. Res.*, *91*, 8411–8427, 1986.

Ralph, E. A., K. Bi, P. P. Niiler, and Y. du Penhoat, A Lagrangian description of the western equatorial Pacific response to the wind burst of December 1992: Heat advection in the warm pool, *J. Clim.*, *10*, 1706–1721, 1997.

Rasmusson, E. M., and T. H. Carpenter, Variations in tropical sea surface temperature and surface wind fields associated with the southern oscillation/El Niño, *Mon. Weather Rev.*, *110*, 354–384, 1982.

Roemmich, D., M. Morris, W. R. Young, and J. R. Donguy, Fresh equatorial jets, *J. Phys. Oceanogr.*, *24*, 540–558, 1994.

Shin, K.-S., G. R. North, Y.-S. Ahn, and P. A. Arkin, Time scales and variability of area-averaged tropical oceanic rainfall, *Mon. Weather Rev.*, *118*, 1507–1516, 1990.

Short, D. A., P. A. Kucera, B. S. Ferrier, J. C. Gerlach, S. A. Rutledge, and O. W. Thiele, Shipboard radar rainfall patterns within the TOGA COARE IFA, *Bull. Am. Meteorol. Soc.*, *78*, 2817–2836, 1997.

Smyth, W. D., D. Hebert and J. N. Moum, Local ocean response to a multiphase westerly wind burst, 2, Thermal and freshwater responses, *J. Geophys. Res.*, *101*, 22,513–22,533, 1996.

Soloviev, A., and R. Lukas, Sharp frontal interfaces in the near-surface layer of the ocean in the western equatorial Pacific warm pool, *J. Phys. Oceanogr.*, *27*, 999–1017, 1997a.

Soloviev, A., and R. Lukas, Observation of large diurnal warming events in the near-surface layer of the western equatorial Pacific warm pool, *Deep Sea Res., Part I*, *44*, 1055–1079, 1997b.

Spencer, R. W., Global oceanic precipitation from the MSU during 1979–92 and comparisons to other climatologies, *J. Clim.*, *6*, 1301–1326, 1993.

Sprintall, J., and M. McPhaden, Surface layer variations observed in multiyear time series measurements from the western equatorial Pacific, *J. Geophys. Res.*, *99*, 963–979, 1994.

Sprintall, J., and M. Tomczak, Evidence of the barrier layer in the surface layer of the tropics, *J. Geophys. Res.*, *97*, 7305–7316, 1992.

Thiele, O. W., M. J. McPhaden, and D. A. Short, Optical rain gauge performance, in *Proceedings of the Second Workshop on Optical Rain Gauge Measurements, NASA Conf. Publ.*, *3288*, 76 pp., 1994.

Tomczak, M., Salinity variability in the surface layer of the western Pacific Ocean, *J. Geophys. Res.*, *100*, 20,499–20,515, 1995.

Vialard, J., and P. Delecluse, An OGCM study for the TOGA decade, Part II, Barrier-layer formation and variability, *J. Phys. Oceanogr.*, *28*, 1089–1106, 1998.

Wang, T., and J. D. Crosby, Taking rain gauges to sea, *Sea Technol.*, *34*, 62–65, 1993.

Webster, P. J., and R. Lukas, TOGA COARE: The Coupled Ocean-Atmosphere Response Experiment, *Bull. Am. Meteorol. Soc.*, *73*, 1377–1417, 1992.

Wijesekera, H. W., and M. C. Gregg, Surface layer response to weak winds, westerly bursts, and rain squalls in the western Pacific Warm Pool, *J. Geophys. Res.*, *101*, 977–997, 1996.

Wijesekera, H. W., C. A. Paulson, and A. Huyer, The effect of rainfall on the surface layer during a westerly wind burst in the western equatorial Pacific, *J. Phys. Oceanogr.*, in press, 1998.

Zhang, C., Atmospheric intraseasonal variability at the surface in the western Pacific Ocean, *J. Atmos. Sci.*, *53*, 739–758, 1996.

M. F. Cronin and M. J. McPhaden, NOAA, Pacific Marine Environmental Laboratory, 7600 Sand Point Way NE, Seattle, WA 98115 (e-mail: cronin@pmel.noaa.gov; mcphaden@pmel.noaa.gov)